Wounding triggers invasive progression in human basal cell carcinoma

Laura Yerly[1,a], Massimo Andreatta[2,3a], Josep Garnica[2,3], Jeremy Di Domizio[1], Michel Gilliet[1], Santiago J. Carmona[2,3,b*], François Kuonen[1,b,c*]

[1] Department of Dermatology and Venereology, Lausanne University Hospital Center, CH-1011 Lausanne, Switzerland

[2] Department of Oncology, Ludwig Institute for Cancer Research, Lausanne Branch, CHUV and University of Lausanne, 1011, Lausanne, Switzerland. AGORA Cancer Research Center, 1005, Lausanne, Switzerland

[3] Swiss Institute of Bioinformatics, 1015, Lausanne, Switzerland

[a] These authors contributed equally

[b] Co-last, senior authors

[c] Lead contact

[*]Correspondence: santiago.carmona@unil.ch, francois.kuonen@chuv.ch

Abstract

The interconnection between wound healing and cancer has long been recognized, as epitomized by the expression “cancer is a wound that does not heal”. However, the impact of inducing a wound, such as those from biopsies, on the progression of established tumors remains largely unknown. In this study, we examine the transcriptional heterogeneity of cancer cells in human basal cell carcinoma (BCC) and identify a wound response-associated gene program as a prominent feature of invasive cancer cells. We find that invasive cancer cells are prevalent in ulcerated BCC tumors and exhibit a distinctive spatial organization. To explore the causal relationship between wounding and cancer progression, we compare tumors at baseline and one week after biopsy. Our results reveal that biopsy collection locally induces a transcriptional switch in cancer cells from an indolent to an invasive state. Notably, this progression is coupled with the reprogramming of cancer-associated fibroblasts, which adopt a transcriptional state characteristic of therapy-resistant BCC. This study provides evidence that wounding triggers invasive progression of established human tumors and warrants further research on the potentially harmful effects of biopsies and wound-inducing treatments.

Keywords basal cell carcinoma, tumor invasion, cancer progression, cancer cell heterogeneity, wound healing response, tumor ulceration, single-cell transcriptomics, gene expression programs, GeneNMF

Introduction

Basal cell carcinoma (BCC), the most frequent cancer in humans, displays extensive inter- and intra-tumoral morphological variability, with histologic patterns that can be classified within a spectrum from nodular to infiltrative[1,2]. The progression of BCC from a nodular to an infiltrative pattern, as typically observed, is most notably marked by a significant increase in invasiveness – a key hallmark of cancer[3] – and associated with growing resistance to standard-of-care therapies[4,5]. The molecular triggers driving nodular to infiltrative transition in BCC are however largely unknown. Previous independent studies showed that infiltrative BCCs are not characterized by distinct somatic genomic alterations[6,7] suggesting that invasive progression might be primarily driven by non-genetic changes. Consistently, we have previously shown that nodular to infiltrative transition is a fast-inducible phenomenon associated with progressive transcriptional changes in cancer cells[8,9]. Here, we aimed to investigate in more detail the association between the transcriptional heterogeneity of BCC cancer cells and invasive progression. We identified a wound response-associated gene program as the most distinctive feature of invasive cancer cells, leading us to investigate the impact of wounding on human BCC.

Results

Cancer cell-intrinsic transcriptional programs underpin invasion patterns in human basal cell carcinoma.

Human BCC tumors, classified histopathologically into nodular or infiltrative types, display extensive intratumoral morphological heterogeneity (**Fig. 1A**). We hypothesized that this intratumoral morphological variability is reflected at the transcriptional level, by distinct patterns of gene expression programs. To identify the gene programs underlying this transcriptional heterogeneity, we first performed an unsupervised meta-analysis of single-cell RNA-seq data from BCC tumors of 11 patients (**Fig. 1B** and **Fig. S1**; **Table S1**) (GSE181907[9]; E-MTAB-13085[10]). Using a gene program discovery approach based on non-negative matrix factorization (see Methods), we identified seven robust gene metaprograms (MP 1 to 7) that consistently explain the cancer cell transcriptional heterogeneity across patients and algorithm initializations (**Fig. 1C**; **Table S2**). Comparison of the identified MPs with those from the comprehensive pan-cancer analysis by Gavish *et al.*[11] revealed that MP1 and MP6 correspond to previously identified cell cycle and (heat-shock) stress response MPs, respectively (**Fig. 1D** and Methods). The remaining MPs did not show significant association with previously reported cancer cell programs. Examination of the most influential genes and gene set enrichment analysis suggested potential roles in cell radial projection for MP2 (*LAMB1* and *LRP8)*; in epidermal differentiation for MP3 (*CLDN4*, *CALML5*, *LGALS7B* and *KRT75*); and in epidermal response to wounding for MP7 (*TIMP1, CHI3L1,* and *IFITM3*) (**Fig. 1D**; **Fig S2A**).

We hypothesized that distinct MP activation patterns might be underpinning invasive progression. To address this, we took advantage of previous results where we identified, using GeoMx spatial transcriptomics, gene signatures of highly-infiltrative

and highly-nodular BCC tumors[9]. These signatures allowed us to calculate a nodular-to-infiltrative (NI) score for each single cancer cell, ranging from -1 in fully nodular to 1 in fully infiltrative BCC cancer cells (see Methods). Next, we examined whether individual MP activities were associated at the single-cell level with the nodular or infiltrative pattern by examining their correlation with the NI score across cells and samples (**Fig. 1E**). MP2 displayed the highest negative correlation. A characteristic feature of nodular BCC is a radially-oriented architecture of the basal layer[1,2], with apical projection of the primary cilium[12], suggesting a potential role of MP2 in nodular pattern formation or maintenance. Interestingly, MP2 also included *LGR5* (**Fig. 1D**), a gene marker for hair follicle stem cells with rapid adaptive capacity during wound healing[13]. In contrast, we found that MP7 displayed the highest positive correlation with NI score (**Fig. 1E**). This correlation was consistent across individual patients (**Fig. S2B**) suggesting an association of this metaprogram with the infiltrative pattern. Using a multivariate linear model, we verified that MP7 was indeed the strongest predictor of the infiltrative score (**Fig. 1F**, see Methods). In sum, we identified cancer cell-intrinsic gene expression programs characterizing BCC cancer cell heterogeneity and found that a gene metaprogram related to the epidermal wound response (MP7) is most strongly associated with BCC invasive progression.

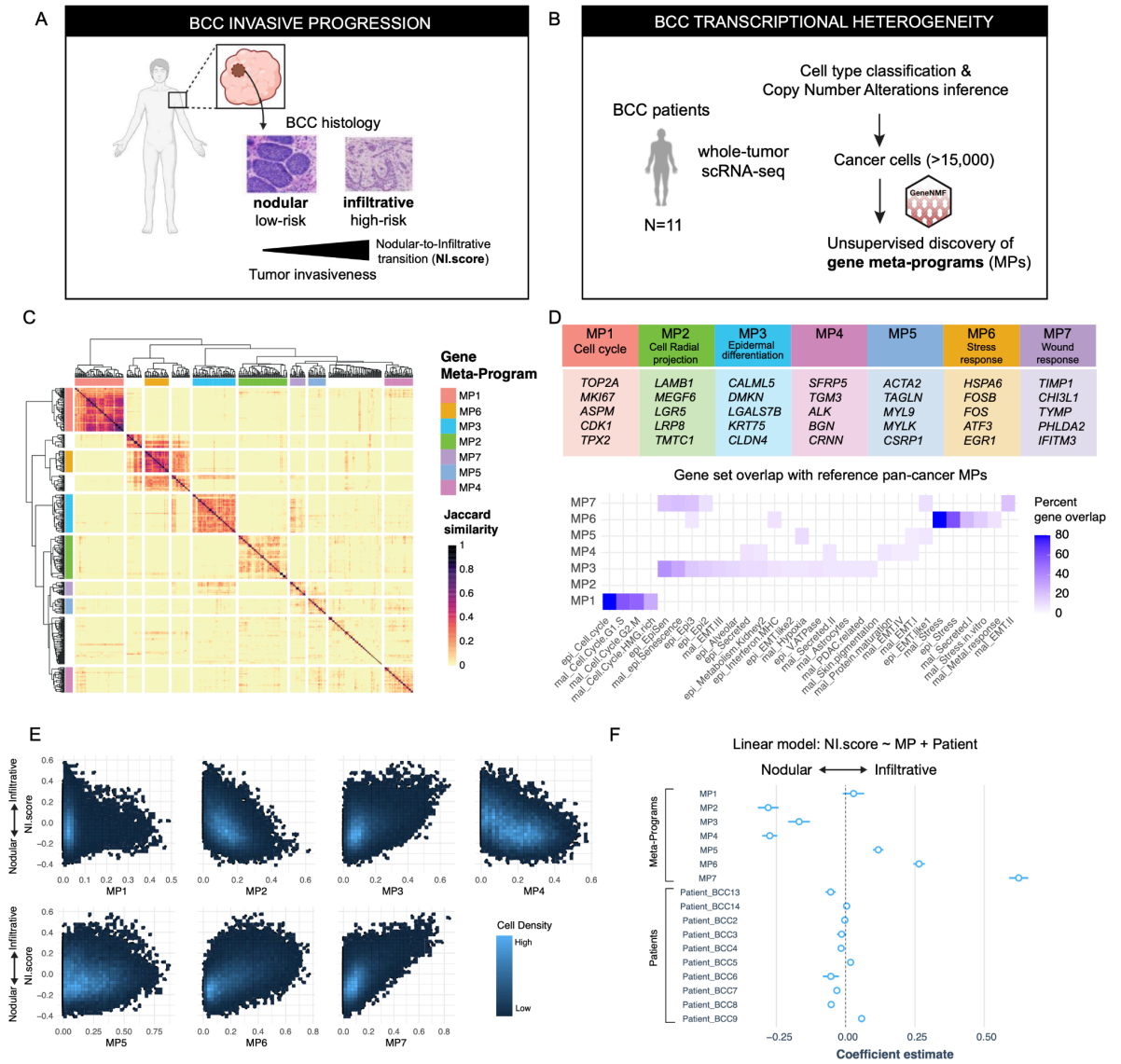

Figure 1. Cancer cell-intrinsic transcriptional programs underpin invasion patterns in human basal cell carcinoma. A) BCC displays histological heterogeneity that can be classified as nodular or infiltrative. The nodular-to-infiltrative score (NI.score) is calculated from gene signatures derived from nodular and infiltrative BCC tumor niches assayed by spatial transcriptomics. **B)** To study BCC cancer cells transcriptional heterogeneity, whole-tumor scRNA-seq patients was performed for 11 patients; cancer cells were computationally identified and subjected to gene meta-programs discovery using a new tool described in this paper, called GeneNMF (https://CRAN.R-project.org/package=GeneNMF). **C)** Pairwise similarity (Jaccard index) between individual gene programs, defining 7 clusters of similar and non-redundant programs, termed metaprograms (MP). **D)** Top 5 genes specific for each MP, and percent gene overlap between the 7 MPs and the reference pan-cancer metaprograms in malignant (mal) and normal epithelial (epi) cells defined by Gavish et *al.*[11]. **E)** Signature scores for MP gene sets vs. NI.score, calculated for individual cancer cells from the 11 BCC patients; color represents cell density. **F)** Coefficient estimates for a linear model aiming to predict the NI.score from MP signature scores

and accounting for the patient of origin; note that, because “Patient” is a categorical variable, it must be converted into a contrast matrix of n-1 levels, therefore coefficients are reported for n-1 patients. MP, meta-program.

Cancer cell-intrinsic gene programs associated with invasive BCC are spatially organized.

To assess whether MPs act independently or in a coordinated fashion, we evaluated the co-expression patterns of MPs in single BCC cancer cells (**Fig. 2A**). As expected, MP7 activity was most negatively correlated with MP2, a nodular-associated (infiltrative-antagonistic) program. Conversely, the activity of MP7 was most positively correlated with epidermal differentiation program MP3 (**Fig. 2A**). In fact, these two MPs shared a fraction of genes (**Fig. S3 A-C**), including some genes previously shown to be up-regulated in infiltrative cancer cells, such as *KRT6A*, *INHBA* and S100A7[9]. However, when considering MP-specific genes, such as Tissue Inhibitor of Metalloproteinases 1 (*TIMP1*) for MP7 and Claudin 4 (*CLDN4*) for MP3 (**Fig. 1D** and **Fig. S3C**), we found a largely mutually exclusive activation pattern, magnified within the infiltrative, *KRT6A*-expressing tumor cells (**Fig. 2B**, **Fig. S3B**). This suggested that there might be two functionally distinct cancer cell populations in the tumor infiltrative niche, possibly with distinct spatial organization. To test this, we assembled a collection of BCC tumor samples, displaying nodular and infiltrative patterns. We first verified that tumor morphological complexity (see Methods) – a hallmark of infiltrative BCC – was higher in selected infiltrative compared to nodular areas (**Fig. 2C**). Infiltrative areas also displayed increased expression level of the infiltrative marker *KRT6A*, measured by RNA FISH (**Fig. S3D**). As predicted, staining for MP7- and MP3-specific markers (*TIMP1* and *CLDN4* respectively) revealed a distinctive spatial organization of the infiltrative niche (**Fig. 2D**). *TIMP1*-high tumor cells were

found exclusively in the infiltrative niches and predominantly in contact with the basement membrane zone (BMZ) (i.e. with highest expression at an average distance of 0 cells from the BMZ; **Fig. 2 E-F**). Instead, *CLDN4*-high tumor cells were found in both nodular and infiltrative niches, but with a distinct spatial organization in the infiltrative niches. Whereas *CLDN4* was expressed in nodular cores, *CLDN4*-high tumor cells in infiltrative niches were predominantly found at 1-cell distance from the BMZ, in close contact with *TIMP1*-high cells (**Fig. 2 E-F**).

Altogether, we found that MP7 and MP3 are activated in adjacent populations of cancer cells. In particular, MP7 cells tend to surround MP3 cells, forming a spatial architecture specifically found within the infiltrative niche of BCC.

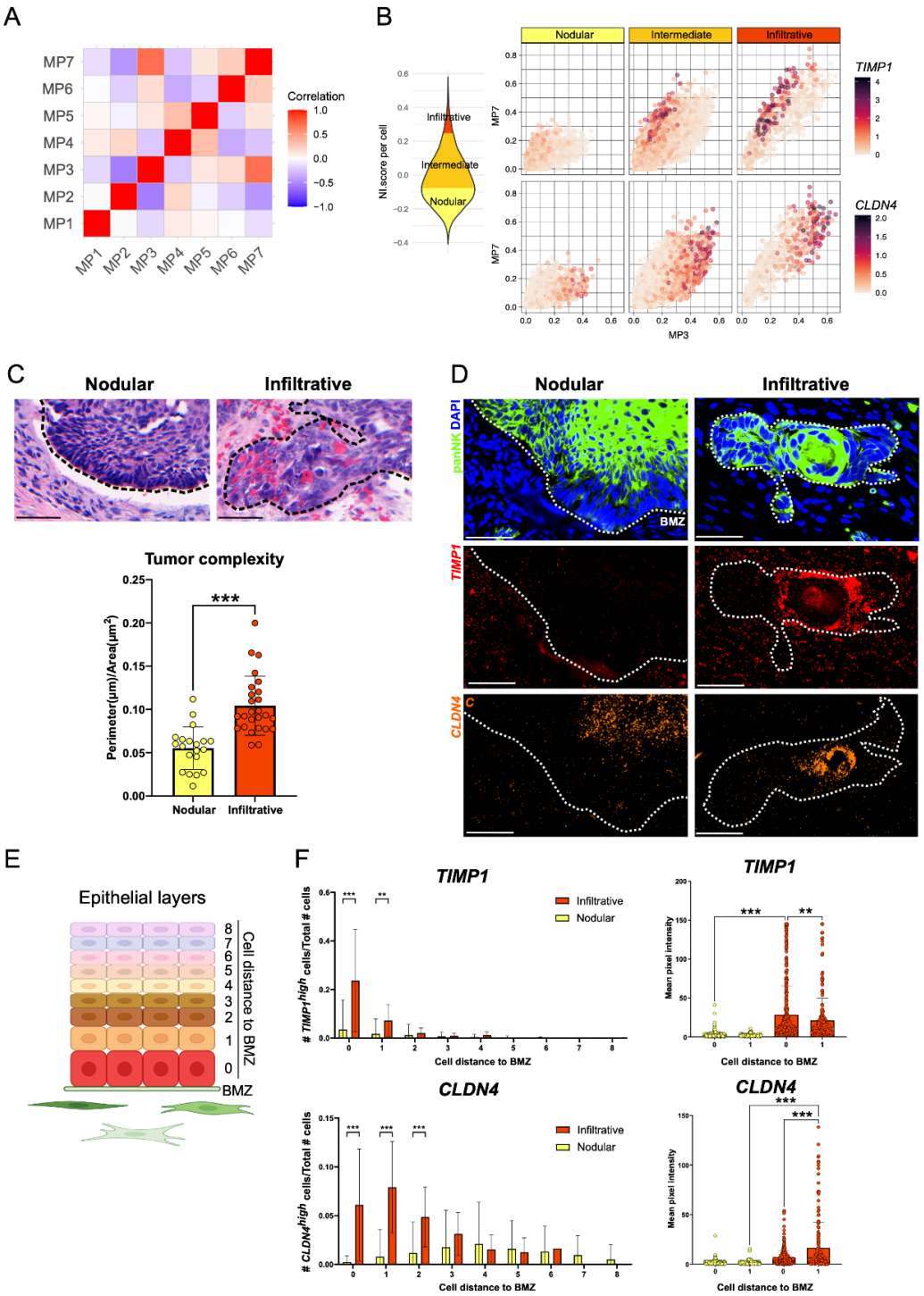

Figure 2. Cancer cell-intrinsic gene programs associated with invasive BCC are spatially organized. A) Pairwise correlation of MP scores at the single-cell level in >15'000 cancer cells from 11 BCC patients. **B)** Signature scores of MP3 vs. MP7 for cancer cells classified as nodular, intermediate, or infiltrative. Cells are classified in these three categories by binning the observed NI.score range into three equal intervals. Cells are colored by the normalized expression of *TIMP1* (top) and *CLDN4* (bottom). **C)** Representative scan H&E images of nodular and infiltrative patterns. Scale bars indicate 50 µm. Bar graph represents the mean tumor complexity of

nodular and infiltrative areas (*N*≥20 areas/condition) measured across N=12 BCCs. Horizontal bars indicate the mean ± SD. p-values were calculated by unpaired two-sided Student's *t* test. **D)** Representative scan images of nodular and infiltrative BCC areas stained with DAPI (blue), pan-cytokeratin (green), *TIMP1* (red) and *CLDN4* (orange). White dotted lines depict the basement membrane zone (BMZ). Scale bars indicate 50 µm. **E)** Schematic of the cells located at 0-8 cell(s) distance from BMZ, used for quantification in the next panel. **F)** Left panel: bar graph representing the mean number of *TIMP1*^{high} or *CLDN4*^{high} cells at a certain distance (0-8 cell(s)) to the BMZ in nodular and infiltrative areas (*N*≥20 areas/condition) measured across 12 BCCs. Horizontal bars indicate the mean ± SD. Significant pairwise comparisons between nodular and infiltrative patterns are highlighted. p-values were calculated by unpaired two-sided Student's *t* test. Right panel: bar graph representing the mean pixel intensity of *TIMP1* and *CLDN4* in tumor cells located at 0 and 1 cell-distance from BMZ in nodular and infiltrative areas measured in *N*≥150 cells/condition across *N*=11 BCCs. Each point represents a cell (see Methods). Horizontal bars indicate the mean ± SD. p-values were calculated one-way ANOVA and Tukey's multiple comparisons test (p-value: * <0.05, ** <0.01, *** <0.001). BMZ, basement membrane zone; MP, meta-program.

Ulcerated BCC tumors display invasive features.

Injury to the epithelial barrier, or ulceration, is a salient feature of BCCs[1,14,15]. Although tumor ulceration has been associated with poor survival in metastatic skin cancers[16,17], the association of ulceration with invasive features in BCC tumors has not been explored. Given the presumed role of both MP7-specific genes (*TIMP1*[18] and *IFITM3*[19]), and MP3-specific genes (*CLDN4*[20], *CALML5*[21], *LGALS7B*[22]) in the epidermal response to injury, we hypothesized that these MPs would be upregulated and embedded in an infiltrative morphology in ulcerated compared to non-ulcerated tumor areas. To investigate this, we unbiasedly extracted BCC samples classified as nodular and ulcerated based on histopathological reports from our tissue biobank (see Methods). We found that in nearly all samples, despite prominent nodular characteristics, ulcerated areas displayed increased invasiveness, reflected by higher tumor complexity (**Fig. S4A-B**) and upregulated expression of *KRT6A* in tumor cells (**Fig. S4C-E**). Notably, we found a strong upregulation of *TIMP1* (MP7 specific

marker) and *CLDN4* (MP3 specific marker) at 0- and 1-cell distance from the BMZ, respectively (**Fig. S4F-G**), recapitulating the characteristic spatial organization of infiltrative BCC. We refer to this transcriptional and spatial tumoral pattern as the "wound-related invasive" (WRI) architecture and established it as a hallmark of ulcerated BCC tumors.

Tumor wounding triggers invasive progression in human BCC.

Invasive BCC tumors may ulcerate as a consequence of outgrowing their blood supply. At the same time, it is an intriguing possibility that wounding might be a driving factor for further invasiveness, establishing a self-sustaining positive feedback loop for tumor progression. To test whether wounding could trigger nodular to infiltrative transition in human BCC, we designed a longitudinal experiment to compare tumors taken before and after inducing a wound by punch biopsy. We selected four patients with non-ulcerated, non-biopsied, suspected nodular BCC tumors. For each patient, we collected three samples: *i)* from baseline (first, diagnostic biopsy), and 1 week later *ii)* from the previously biopsied, wounded site, and *iii)* from a distant, unwounded site in the same tumor (**Fig. 3A**). All samples were subjected to RNA FISH and H&E staining, and two of them, to scRNA-seq. Notably, we found that one week after punch biopsy-induced wounding, the wounded tumor sites displayed a transition from a nodular to an infiltrative morphology, as reflected by increased morphological complexity and higher expression of *KRT6A* in tumor cells compared to baseline or unwounded tumor sites (**Fig. 3B** and **Fig. S5A**). Moreover, compared to the baseline or the unwounded sites, cancer cells in the site of induced wound significantly upregulated the MP7 gene program (**Fig. 3C**). Notably, the range of MP7 activation upon wounding was similar to the MP7 range observed between non-invasive and invasive BCC tumors (**Fig. 3C, Fig. S5B**). Consistently,

individual MP7-specific marker genes, such as *TIMP1, CHI3L1*, and *IFITM3* were significantly up-regulated upon wounding while several MP2-specific marker genes were down-regulated upon wounding in the two patients for which scRNA-seq data were generated (**Fig. S5B-D**). In fact, MP2 and MP7 marker genes were among the most differentially expressed genes in the wounded vs. baseline or unwounded conditions (**Fig. 3D** and **Fig. S5D**), indicating that these gene programs indeed captured the most prominent transcriptional changes that are induced in cancer cells upon wounding. In contrast, MP3 did not show a robust modulation upon wounding (**Fig. S5B-C**), consistent with our previous results showing that the spatial organization of this program, rather than its global activation, is associated with invasive progression. To investigate the spatial organization of wounded tumors, we stained the samples for *TIMP1* and *CLDN4*. Remarkably, we found that tumor wounding locally induced the characteristic spatial organization of the WRI architecture, as reflected by the induced expression of both *TIMP1* and *CLDN4* at the basal and suprabasal layers, respectively (**Fig. 3E-F**). Altogether, our data show that injury locally triggers a cancer cell switch from a non-invasive to an invasive state. This observation supports the role of wounding as a driver of invasive progression in human BCC.

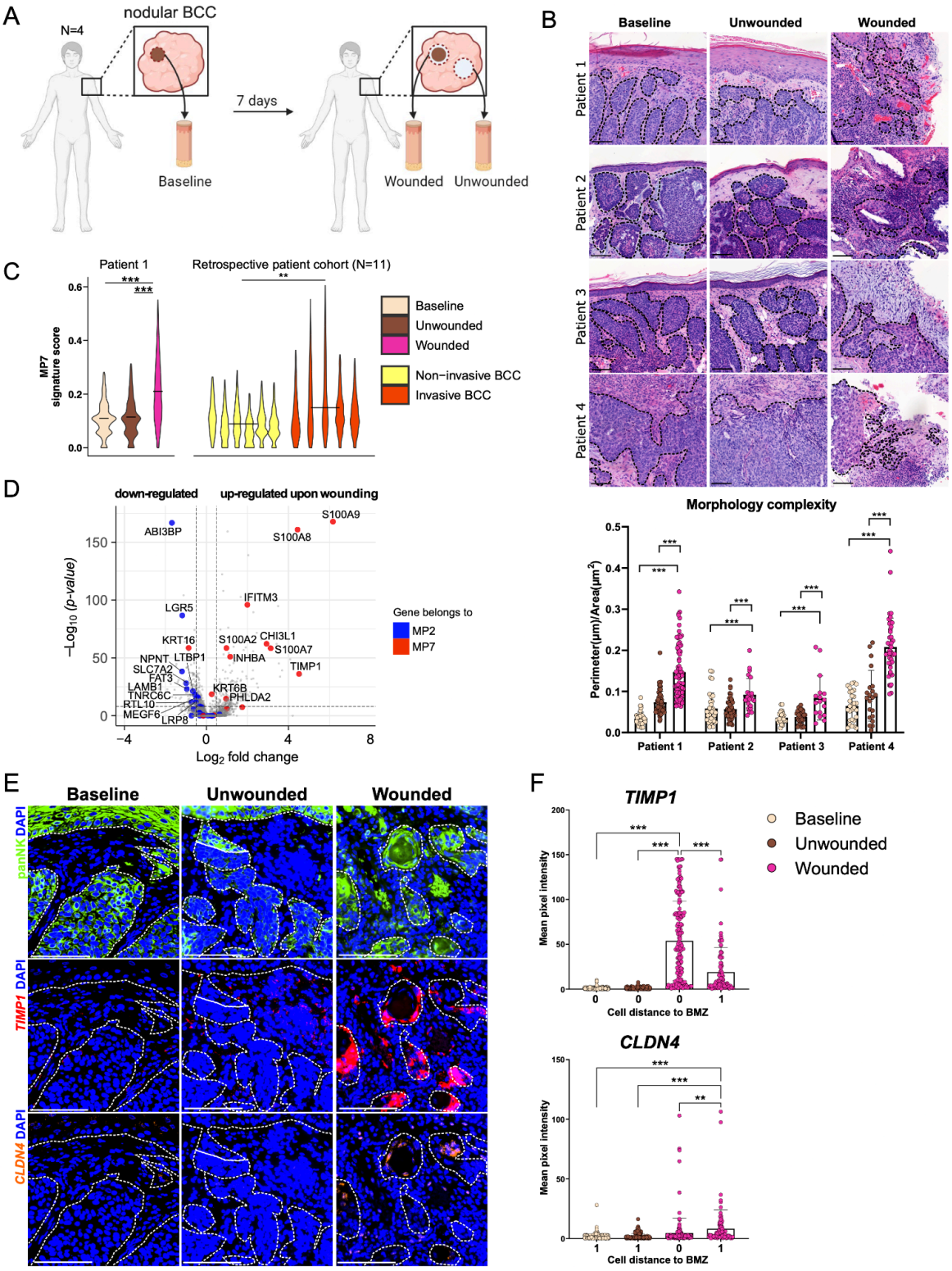

Figure 3. Tumor wounding triggers invasive progression in human BCC. A) Experimental design. For each patient, samples were collected with a first biopsy (Baseline) and 1 week later from the previously biopsied site (Wounded) and at a distant site (Unwounded) in the same tumor. **B)** Representative scan of H&E images from 4 BCC patients at baseline and 7 days later in the wounded and unwounded areas. Black dotted lines depict the

basement membrane zone (BMZ). Scale bars indicate 100 µm. Bar graph represents the mean tumor complexity in baseline, unwounded and wounded biopsies of the 4 BCC patients. Each dot represents a measured tumor area ($N \geq 17$ tumor areas/condition). Horizontal bars indicate the mean ± SD. p-values were calculated by one-way ANOVA and Tukey's multiple comparisons test. **C)** Distribution of MP7 signature scores in BCC cancer cells sequenced by scRNA-seq in (left) Baseline, Unwounded and Wounded samples of patient 1, and (right) BCC patients retrospective cohort where tumors were globally classified as non-invasive (predominantly nodular, N=6) and invasive (predominantly infiltrative, N=5) (data for patient 2 in Figure S5). Black lines represent the mean of MP7 signature score for each sample type. P-values were calculated by either Wilcoxon rank-sum test (left) or t-test (right) (* adj. p-value <0.05, *** adj. p-value <0.001). **D)** Differentially expressed genes between Wounded sample vs. Baseline/Unwounded samples for a representative patient (data for second patient in Figure S5). Genes contained in MP2 and MP7 are highlighted blue and red respectively. **E)** Representative scan images of Baseline, Unwounded and Wounded biopsies stained with DAPI (blue), pan-cytokeratin (green), *TIMP1* (red) and *CLDN4* (orange). White dotted lines depict the BMZ. Scale bars indicate 100 µm. **F)** Bar graph representing the mean pixel intensity of *TIMP1* and *CLDN4* at 0 and 1 cell distance from BMZ in baseline, unwounded and wounded measured in $N \geq 90$ cells/condition across 4 patients with BCC. Each dot represents one cell. Horizontal bars indicate the mean ± SD. p-values were calculated by one-way ANOVA and Tukey's multiple comparisons test (p-value: * <0.05, ** <0.01, *** <0.001). BMZ, basement membrane zone.

Wounding induces a cancer-associated fibroblast state characteristic of invasive and advanced BCC.

Our results revealed a transcriptional switch and spatial reorganization of cancer cells that is characteristic of both chronically invasive BCC tumors and (initially) non-invasive BCC tumors that were wounded a week before. To investigate whether the interconnection between these two conditions extends beyond cancer cells, we next examined the changes induced by wounding on the tumor microenvironment.

Compared to baseline, wounded samples displayed a ~10 fold increase in the relative abundance of cancer-associated fibroblasts (CAFs) and immune cells (including T cells, monocytes, macrophages and dendritic cells), as well as a modest increase of endothelial cells and a decrease of pericytes (**Fig. 4A**). These results indicate wound-triggered inflammation and fibroblast expansion. In addition to

proportional changes, tumor-infiltrating stromal and immune cells displayed altered transcriptional profiles in response to wounding, especially for CAFs (**Fig. S6A**). CAFs upregulated the expression of metalloproteases (*MMP3* and *MMP1*), glycolysis-related genes (*GAPDH*, *ENO1*, *BASP1*, *PKM*, and *TPI1*), contractile protein genes (*TPM2*), and cellular stress genes (*NFKBIA* and *IER3*) (**Fig. 4B and Table S3**). These results indicate that BCC tumor wounding induces, within one week, a distinct CAF state characterized by profound changes in metabolism, contractility, and extracellular matrix remodeling.

The WRI switch in cancer cells, captured by MP7, appears in nodular (non-invasive) BCC tumors one week after wounding (**Fig. 3**) and is observed permanently in infiltrative (invasive) BCC tumors (**Fig. 3C**; **Fig. S6B**). We thus wondered whether the acute, wound-induced CAF reprogramming is also a shared feature of infiltrative BCC tumors. To test this hypothesis, we constructed a signature from the genes differentially expressed by CAFs upon wounding ("wound-responding" CAFs; **Table S3**), and used it to query transcriptional profiles of CAFs in our retrospective BCC patients cohort (see Methods). The "wound-responding" CAF score was significantly higher in invasive BCC compared to non-invasive BCC or normal adjacent skin samples (**Fig. 4C, Fig. S6C, D**). Consistently, it was also significantly higher in intratumoral stromal spots within infiltrative niches compared to stromal spots within nodular niches of non-previously biopsied tumors (**Fig. 4D**). Notably, human samples from advanced, hedgehog inhibitor-resistant BCC[23], and from cutaneous squamous cell carcinoma (cSCC) – a more aggressive, keratinocyte-derived cancer type[24] – displayed the highest "wound-responding" CAF scores and cancer cell-intrinsic MP7 activation (**Fig. 4C**, **Fig. S6B,** see Methods). These data indicate that the CAF reprogramming induced acutely upon biopsy largely overlaps with the differences

observed between non-invasive and invasive BCC tumors (further exacerbated in advanced BCC) and suggest that the invasive alterations triggered by induced wounding may persist over time and lead to poorer prognosis.

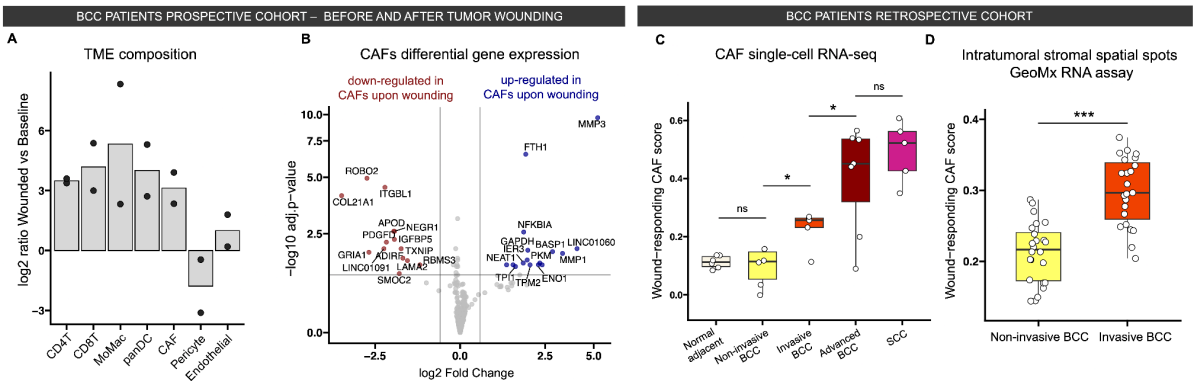

Figure 4. Wounding induces a cancer-associated fibroblast state characteristic of invasive and advanced BCC. A) Ratio of relative abundances of tumor microenvironment (TME) cell types (annotated by scGate[25]) with respect to cancer cells, calculated between Wounded and Baseline paired samples (log2 scale, N=2). Bars represent the mean ratio for each cell type**. B)** Differentially expressed genes in CAFs from Wounded (N=2) vs. baseline (N=2) and Unwounded (N=2) samples. Y axis shows -log10 of adjusted p-values, with a threshold at adj. p-val = 0.05. X axis shows log2 expression fold-change, with thresholds at |log2 fold-change| > 0.5. **C)** Mean UCell scores for wound-responding cancer-associated fibroblast (CAF) signature in human samples of different conditions (on the X-axis): non-cancer, adjacent skin samples ("Normal adjacent", N=6), non-invasive BCCs (N=6), invasive BCCs (N=5), advanced, Hedgehog inhibition (HHI)-therapy resistant BCC (N=7, samples from Yost et *al.*[23]), and squamous cell carcinomas (N=5, samples from Ji et *al.*[26]). **D)** Mean UCell scores for the wound-responding CAF signature in 47 spatial GeoMx stromal spots from 12 independent samples of non-invasive/nodular (N=24) and invasive/infiltrative (N=23) BCC human tumors with no previous biopsy. TME, tumor microenvironment; SCC, squamous cell carcinoma; CAF, cancer-associated fibroblast. p-values were calculated for the indicated comparisons using one-sided t-tests, and adjusted for multiple comparisons using the false discovery rate (FDR) method. (ns = non-significant, * adj. p-value <0.05, *** adj. p-value <0.001)

Discussion

There are remarkable similarities between cancer hallmarks and wound healing[3,27]. While the effect of wound-induced inflammation on early stages of tumor formation has been well documented[28–34], it is unclear how wounding can impact cancer cell progression in established tumors.

In this study, we showed that wounding induced by biopsy collection in BCC patients produces a transcriptional switch in cancer cells from a non-invasive to an invasive state. We found that invasive cancer cells are prevalent in ulcerated BCC tumors and that they are organized in a “wound-related invasive” (WRI) spatial architecture with characteristic expression of gene programs. In particular, MP7 and MP3 include genes implicated in epithelial cell migration (e.g. *TNC*, *TIMP1*, *MMP1, ITGAV, ITGB6*) and epidermal barrier restoration (e.g. *CLDN4*, *DSG1*, *KRT1*, *KRT77*, *SPRR1B*) respectively, and display a spatial coordination – at the basal and suprabasal layers - that reflects the specific architecture of the wound migrating edge[35–38]. In line with these findings, wound epithelial migrating cells and invasive cancer cells share the expression of *ITGB6* (Integrin Subunit Beta 6) and *ITGAV* (Integrin alpha-V), coding for the fibronectin receptor αVβ6 implicated in adhesion to newly-formed, fibrotic stroma[39,40]. Consistently, BCC invasion is coupled with a CAF state that exhibits predominant extracellular matrix-remodeling features which, similarly to dermal fibroblasts upon tissue injury, may sustain invasive cancer cells by providing a provisional matrix[41,42].

The identification of a wound response-related transcriptional program in cancer cells (MP7) that is active in unwounded invasive BCC tumors and switched on in

non-invasive BCC tumors one week after wounding, raises the possibility of potential common regulators. The inflammatory response is triggered almost immediately upon tissue injury[43–45], and emerges as a potential mechanism. We indeed observe early and broad immune infiltration upon tumor injury, coupled with the expression of inflammatory response genes in cancer cells (like the interferon response gene *IFITM3*). Wound healing, however, relies on redundant pathways for efficient wound closure[46], and thus other mechanisms may be at play. The results raise the question of why the process is not self-limited in cancer, in contrast to normal tissue, and further insights may come from the investigation of discrepancies - rather than commonalities - between cancer and the late-stage of tissue repair.

Beyond the identification of tumor ulceration as a potential clinical indicator of an infiltrative BCC, our data raise questions about the benefit-risk balance of wounding procedures in the clinical practice. Biopsies, the mainstay for diagnosing and grading cancers, as well as physical (surgery, radiotherapy, cryotherapy) or chemical (chemotherapy, photodynamic therapy) therapies induce tissue injury. Our data support a potential deleterious effect of these procedures as they may trigger local progression of residual cancer cells. This observation might explain the noted disparity between histological evaluations of biopsy samples and subsequent excisions in various solid epithelial cancers, including BCC[47–53]. It could also elucidate why tumors that recur after wounding treatments often exhibit increased invasiveness compared to the initial primary tumors[54,55]. Notably, infiltrative BCC display increased resistance to standard-of-care therapies compared to nodular BCC[4,5]. In this context, an important consideration is whether therapies that induce wounds, in addition to

promoting invasion, might trigger resistance of residual cancer cells, as also suggested by clinical studies[56]. Because of the conserved wound response in cancer, we anticipate that future research in wound healing will contribute to the identification of new therapeutic targets to prevent cancer progression.

Study limitations

Due to ethical considerations preventing long delays between diagnosis and treatment, our study does not cover the full dynamics of alterations induced upon wounding, especially their long-term maintenance. Thus, the evidence supporting long-term consequences of the cancer cells transcriptional reprogramming induced by tumor wounding are indirect. Second, the deconvolution of cancer cell heterogeneity is based on a limited cohort of naïve BCC patients eligible for surgical treatment, and, as such, may not fully capture the heterogeneity of advanced BCC.

Acknowledgments

This work was supported by the SNSF fellowship PZ00P3-185926 (F.K.), PROMEDICA Stiftung (F.K.), and SNF fellowship 180010 (S.J.C). We thank the Genomic Technologies Facility (GTF) for the scRNA-seq library preparation and sequencing. F.K. and M.G. are members of the SKINTEGRITY.CH collaborative research consortium.

Author Contributions

L.Y., M. A., S.J.C. and F.K. conceived and designed the study and analyzed the experiments. L.Y. performed the wet-lab experiments. M. A., J.G. and S.J.C. performed the computational analyses. L.Y., M. A., S.J.C. and F.K. wrote the manuscript with comments from co-authors. J.D.D and M.G. provided access to the tissue biobank.

Declaration of interests

The authors declare no competing interests.

Supplemental information

Supplemental Tables

Table S1: Metadata table summarizing patient's characteristics of samples used for scRNAseq analysis.

Data repository	Sample	Location
GSE181907	BCC1	left ear
GSE181907	BCC2	forehead
GSE181907	BCC3	left cheek
GSE181907	BCC4	nose
GSE181907	BCC5	nose
GSE181907	BCC6	ear
GSE181907	BCC7	upper lip
E-MTAB-13085	BCC8	cheek
E-MTAB-13085	BCC9	forehead
E-MTAB-13085	BCC10	temple
E-MTAB-13085	BCC11	temple
E-MTAB-13085	BCC12	ear
E-MTAB-13085	BCC13	cheek
E-MTAB-13085	BCC14	ear
E-MTAB-13085	BCC15	nose
GSE266665	Patient 1 Baseline	neck
GSE266665	Patient 1 Unwounded	neck
GSE266665	Patient 1 Wounded	neck
GSE266665	Patient 2 Baseline	cheek
GSE266665	Patient 2 Unwounded	cheek
GSE266665	Patient 2 Wounded	cheek

Table S2. BCC metaprogram genesets.

Table S3. Wound-responding CAF signatures.

Supplemental Figures

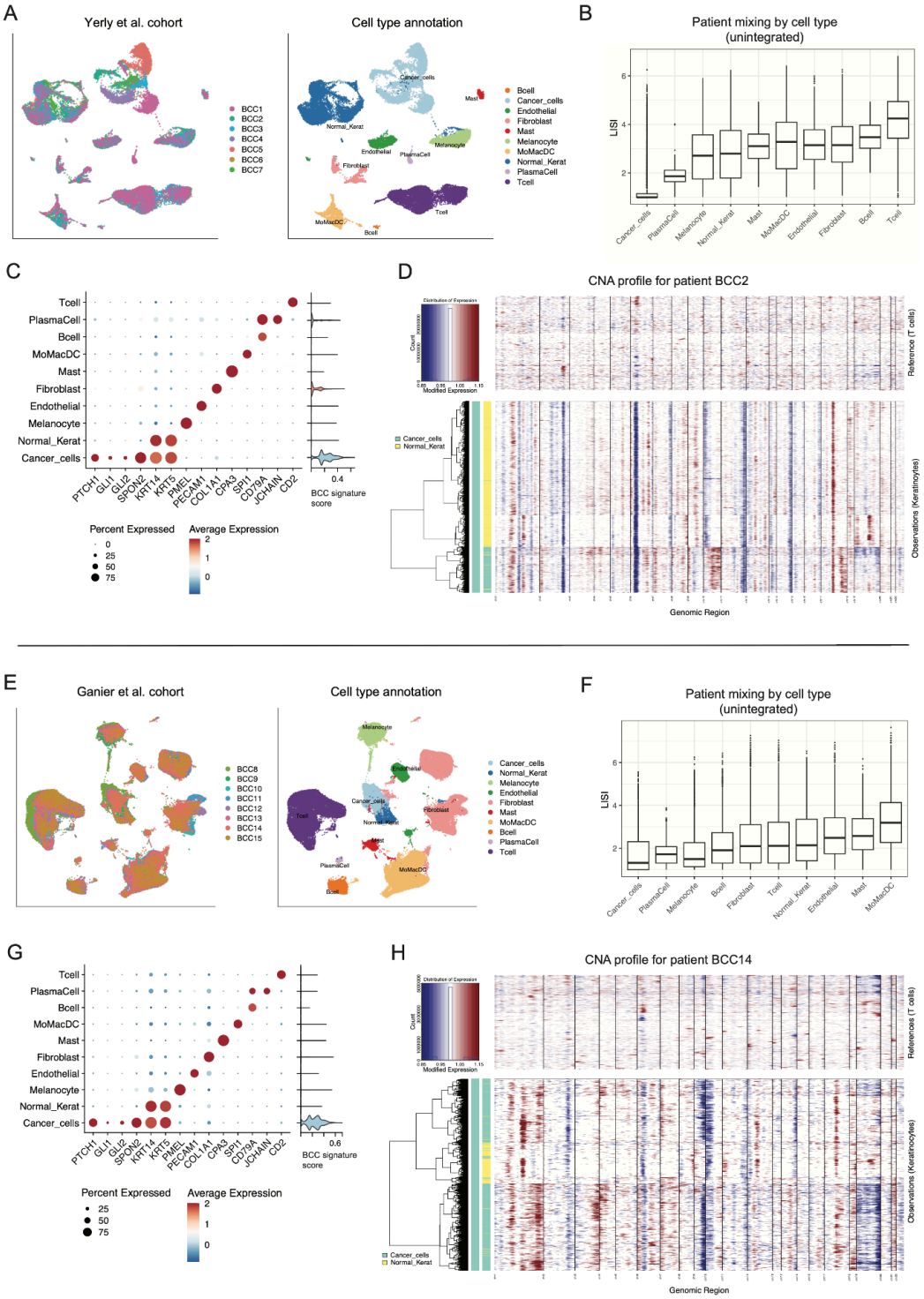

Figure S1. Identification of cancer cells from scRNA-seq of two human BCC cohorts. A) UMAP embeddings by patient and by cell type annotation from the Yerly et al. cohort. Broad annotation was obtained by applying the scGate automated tool and refined by clustering analysis. Identification of cancer cells was performed using three criteria (patient mixing, signature scoring, and copy-number alteration), outlined respectively in panels B, C and D. **B)** Local Inverse Simpson Index (LISI) by cell type, quantifying the number of patients having cells in any given neighborhood of cells. Cancer cells are expected to have more patient-specific transcriptomes than other cell types, and primarily cluster together with cells from the same patient. **C)** Scaled average expression for marker

genes of major TME cell types, and UCell score for a BCC signature defined by Yerly et al. (2022). **D)** Copy-number alteration (CNA) profile for a representative patient, confirming that normal keratinocytes and cancer cells primarily cluster together in terms of inferred CNAs. **E)** UMAP embeddings by patient and by cell type annotation from the Ganier et al. cohort. Broad annotation was obtained by applying the scGate automated tool and refined by clustering analysis. Identification of cancer cells was performed using three criteria (patient mixing, signature scoring, and copy-number alteration), outlined respectively in panels F, G and H. **F)** Local Inverse Simpson Index (LISI) by cell type, quantifying the number of patients having cells in any given neighborhood of cells. Cancer cells are expected to have more patient-specific transcriptomes than other cell types, and primarily cluster together with cells from the same patient. **G)** Scaled average expression for marker genes of major TME cell types, and UCell score for a BCC signature defined by Yerly et al. (2022). **H)** Copy-number alteration (CNA) profile for a representative patient, confirming that normal keratinocytes and cancer cells primarily cluster together in terms of inferred CNAs. CNA, copy number alteration.

A

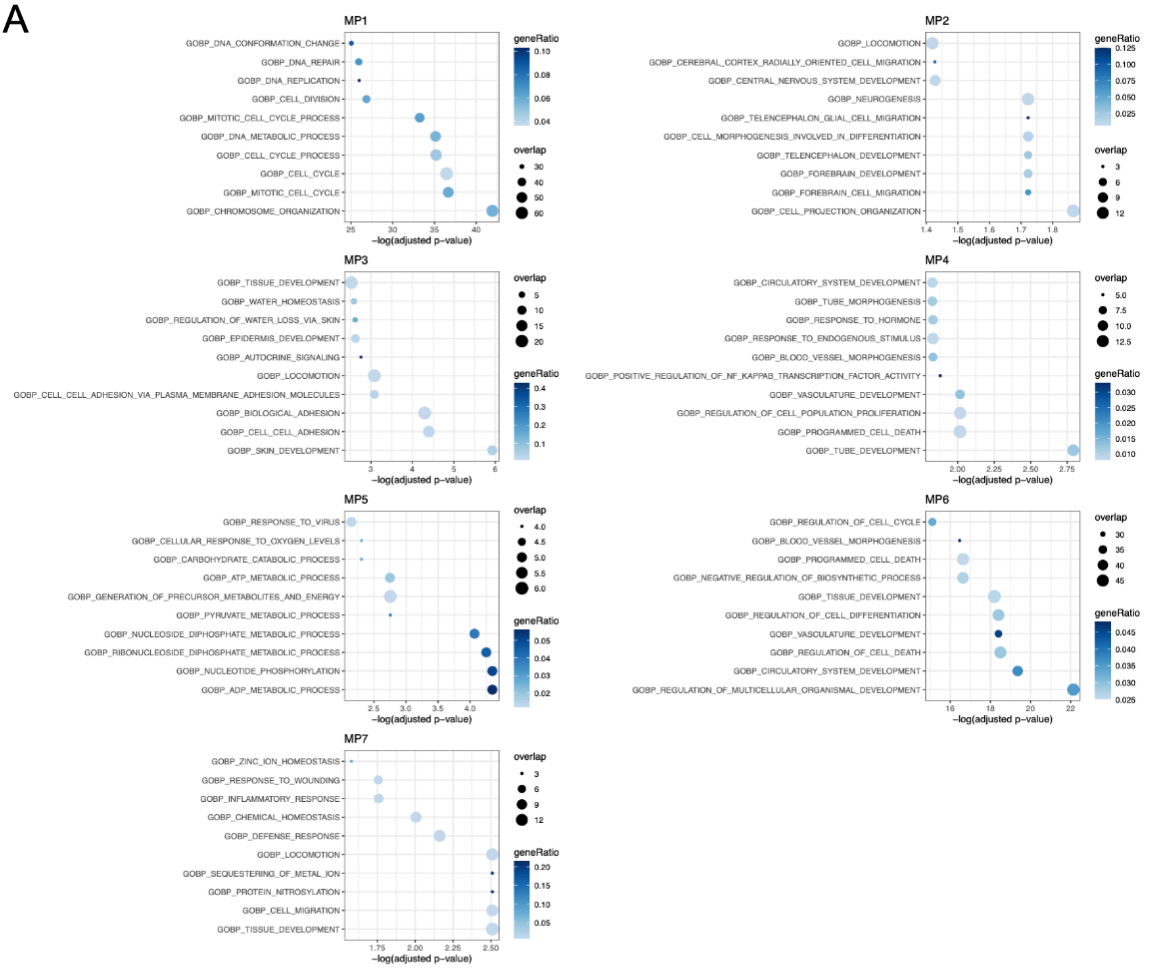
MP1
GOBP_DNA_CONFORMATION_CHANGE
GOBP_DNA_REPAIR
GOBP_DNA_REPLICATION
GOBP_CELL_DIVISION
GOBP_MITOTIC_CELL_CYCLE_PROCESS
GOBP_DNA_METABOLIC_PROCESS
GOBP_CELL_CYCLE_PROCESS
GOBP_CELL_CYCLE
GOBP_MITOTIC_CELL_CYCLE
GOBP_CHROMOSOME_ORGANIZATION
−log(adjusted p−value)
geneRatio
overlap
MP2
GOBP_LOCOMOTION
GOBP_CEREBRAL_CORTEX_RADIALLY_ORIENTED_CELL_MIGRATION
GOBP_CENTRAL_NERVOUS_SYSTEM_DEVELOPMENT
GOBP_NEUROGENESIS
GOBP_TELENCEPHALON_GLIAL_CELL_MIGRATION
GOBP_CELL_MORPHOGENESIS_INVOLVED_IN_DIFFERENTIATION
GOBP_TELENCEPHALON_DEVELOPMENT
GOBP_FOREBRAIN_DEVELOPMENT
GOBP_FOREBRAIN_CELL_MIGRATION
GOBP_CELL_PROJECTION_ORGANIZATION
MP3
GOBP_TISSUE_DEVELOPMENT
GOBP_WATER_HOMEOSTASIS
GOBP_REGULATION_OF_WATER_LOSS_VIA_SKIN
GOBP_EPIDERMIS_DEVELOPMENT
GOBP_AUTOCRINE_SIGNALING
GOBP_LOCOMOTION
GOBP_CELL_CELL_ADHESION_VIA_PLASMA_MEMBRANE_ADHESION_MOLECULES
GOBP_BIOLOGICAL_ADHESION
GOBP_CELL_CELL_ADHESION
GOBP_SKIN_DEVELOPMENT
MP4
GOBP_CIRCULATORY_SYSTEM_DEVELOPMENT
GOBP_TUBE_MORPHOGENESIS
GOBP_RESPONSE_TO_HORMONE
GOBP_RESPONSE_TO_ENDOGENOUS_STIMULUS
GOBP_BLOOD_VESSEL_MORPHOGENESIS
GOBP_POSITIVE_REGULATION_OF_NF_KAPPAB_TRANSCRIPTION_FACTOR_ACTIVITY
GOBP_VASCULATURE_DEVELOPMENT
GOBP_REGULATION_OF_CELL_POPULATION_PROLIFERATION
GOBP_PROGRAMMED_CELL_DEATH
GOBP_TUBE_DEVELOPMENT
MP5
GOBP_RESPONSE_TO_VIRUS
GOBP_CELLULAR_RESPONSE_TO_OXYGEN_LEVELS
GOBP_CARBOHYDRATE_CATABOLIC_PROCESS
GOBP_ATP_METABOLIC_PROCESS
GOBP_GENERATION_OF_PRECURSOR_METABOLITES_AND_ENERGY
GOBP_PYRUVATE_METABOLIC_PROCESS
GOBP_NUCLEOSIDE_DIPHOSPHATE_METABOLIC_PROCESS
GOBP_RIBONUCLEOSIDE_DIPHOSPHATE_METABOLIC_PROCESS
GOBP_NUCLEOTIDE_PHOSPHORYLATION
GOBP_ADP_METABOLIC_PROCESS
MP6
GOBP_REGULATION_OF_CELL_CYCLE
GOBP_BLOOD_VESSEL_MORPHOGENESIS
GOBP_PROGRAMMED_CELL_DEATH
GOBP_NEGATIVE_REGULATION_OF_BIOSYNTHETIC_PROCESS
GOBP_TISSUE_DEVELOPMENT
GOBP_REGULATION_OF_CELL_DIFFERENTIATION
GOBP_VASCULATURE_DEVELOPMENT
GOBP_REGULATION_OF_CELL_DEATH
GOBP_CIRCULATORY_SYSTEM_DEVELOPMENT
GOBP_REGULATION_OF_MULTICELLULAR_ORGANISMAL_DEVELOPMENT
MP7
GOBP_ZINC_ION_HOMEOSTASIS
GOBP_RESPONSE_TO_WOUNDING
GOBP_INFLAMMATORY_RESPONSE
GOBP_CHEMICAL_HOMEOSTASIS
GOBP_DEFENSE_RESPONSE
GOBP_LOCOMOTION
GOBP_SEQUESTERING_OF_METAL_ION
GOBP_PROTEIN_NITROSYLATION
GOBP_CELL_MIGRATION
GOBP_TISSUE_DEVELOPMENT

B

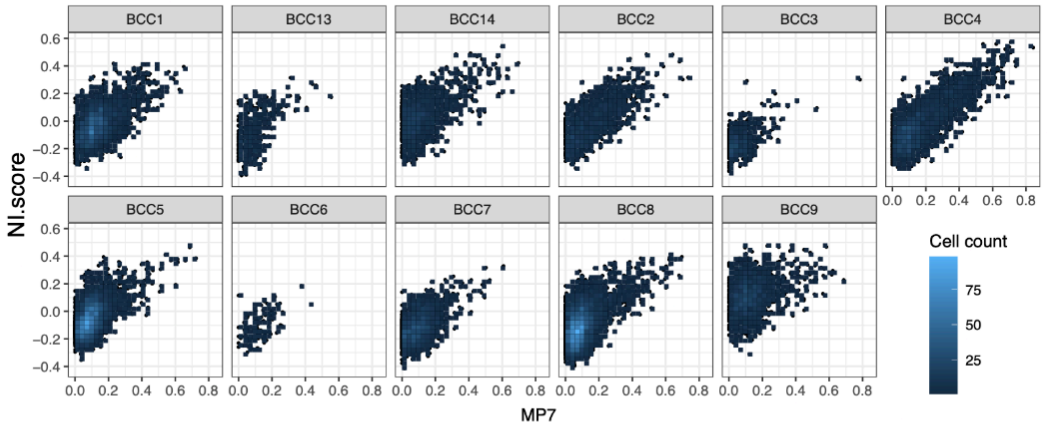
BCC1
BCC13
BCC14
BCC2
BCC3
BCC4
BCC5
BCC6
BCC7
BCC8
BCC9
NI.score
MP7
Cell count
75
50
25

C

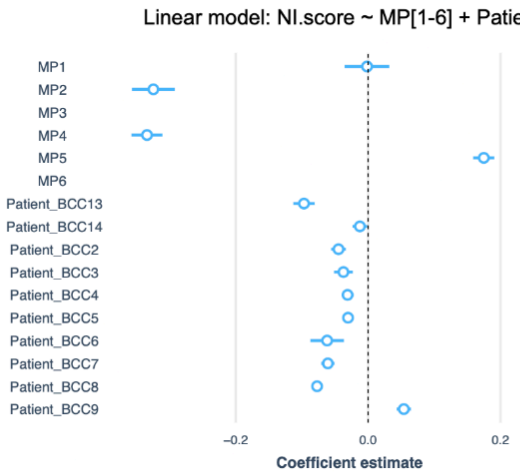
Linear model: NI.score ~ MP[1-6] + Patient
MP1
MP2
MP3
MP4
MP5
MP6
Patient_BCC13
Patient_BCC14
Patient_BCC2
Patient_BCC3
Patient_BCC4
Patient_BCC5
Patient_BCC6
Patient_BCC7
Patient_BCC8
Patient_BCC9
−0.2
0.0
0.2
Coefficient estimate

Figure S2. Characterization of MPs and their relation to NI.score across multiple patients. A) Gene set enrichment analysis (GSEA) between BCC meta-programs and Gene Ontology (GO) gene sets from MSigDB. Dot size is proportional to the number of genes shared between a MP-GO term pair, dot color represents the ratio between the number of shared genes over the total number of genes in the GO signature. **B)** Signature scores in individual cells for MP7 gene sets vs. NI.score, showing their correlation across 11 different patients. **C)** Coefficient estimates for a linear model aiming to predict the NI.score from MP signature scores (all excluding MP7) and accounting for the patient of origin. MP, meta-program.

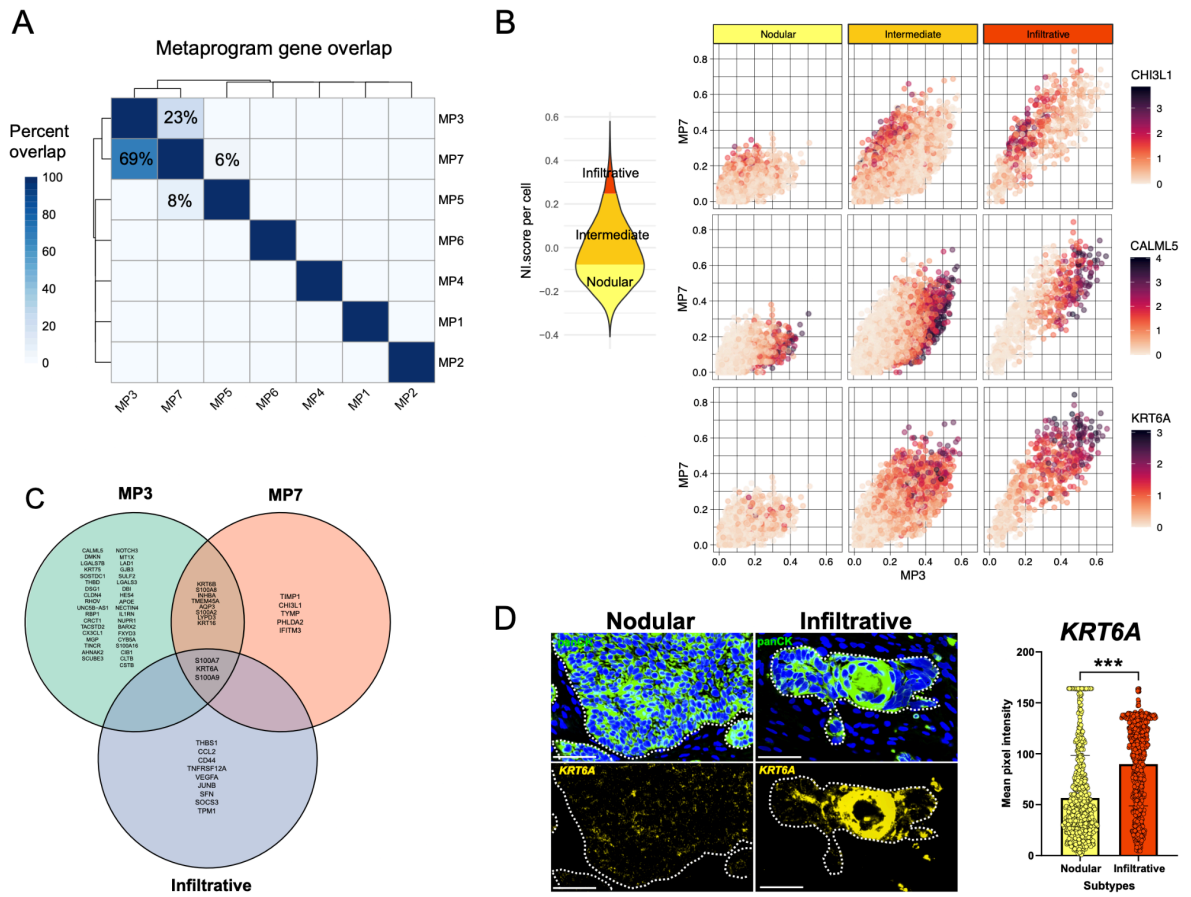

Figure S3. Relationship between wound response MP, epidermal differentiation MP, and the nodular-infiltrative axis. A) Percent gene overlap between pairs of metaprograms, measured as the fraction of genes from meta-program X (row) that are contained in meta-program Y (column). **B)** Signature scores of MP3 vs. MP7 for cells with nodular, intermediate and infiltrative transcriptomics profiles. Cells are classified in these three categories by binning the observed NI.score range into three equal intervals. Cells are colored by the normalized expression of *CHI3L1* (top), *CALML5* (mid) and *KRT6A* (bottom). **C)** Gene overlap between MP3, MP7 and the positive component of the nodular-to-infiltrative signature (Infiltrative). **D)** Representative scan images of nodular and infiltrative areas of BCCs stained with DAPI (blue), pan-cytokeratin (green) and *KRT6A* (yellow). Bar graph represents the mean pixel intensity of *KRT6A* in nodular and infiltrative areas ($N \geq 600$ cells/condition) across N=12 BCCs. White dotted lines depict the basement membrane zone (BMZ). Scale bars indicate 50 µm. Horizontal bars indicate the mean ± SD. p-values were calculated by unpaired two-sided Student's *t* test and stars represent p-value <0.0001. BMZ, basement membrane zone; MP, meta-program.

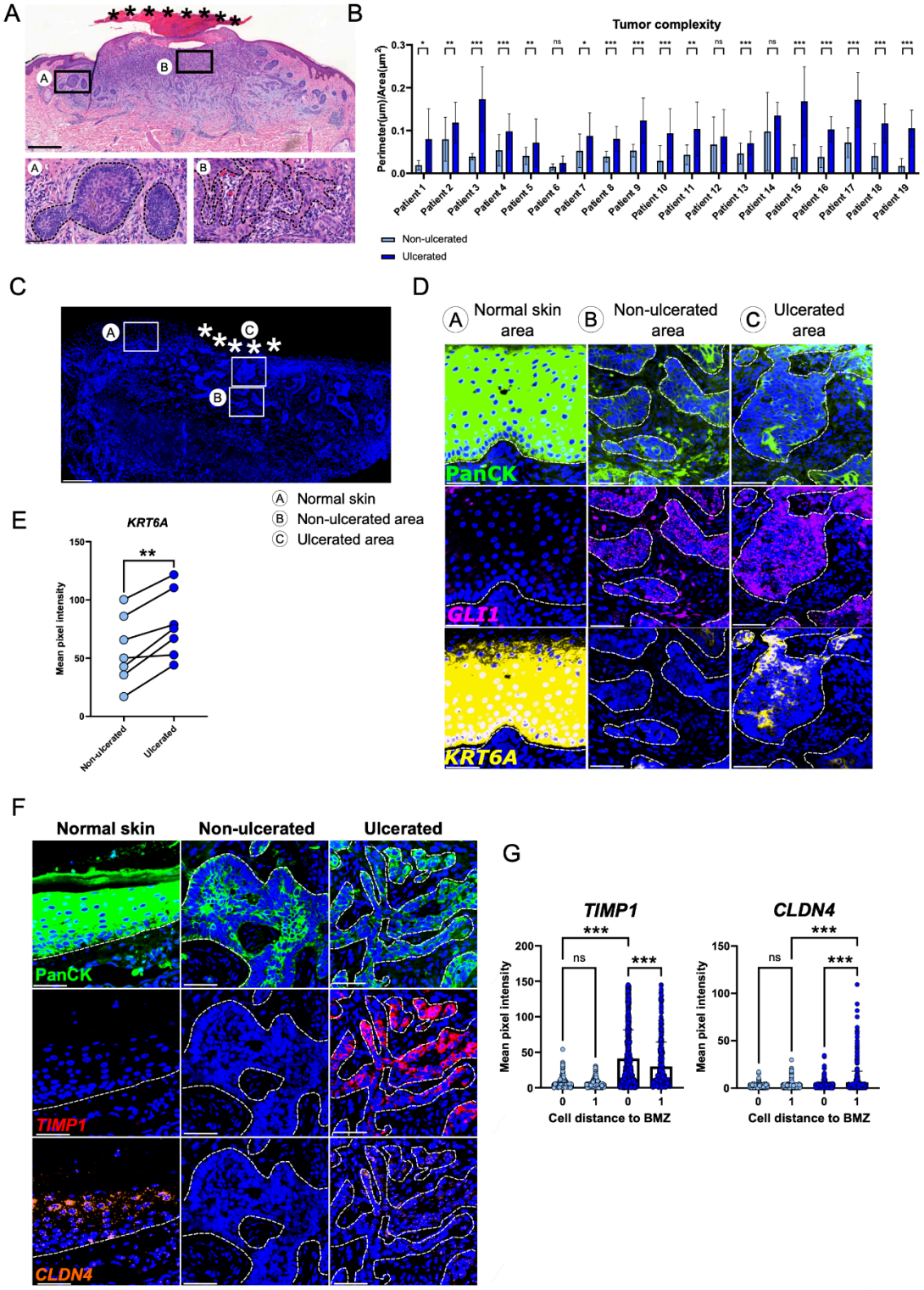

Figure S4. Infiltrative progression as a hallmark of BCC tumor ulceration. A) Representative scan of H&E images of an ulcerated BCC sample in which (A) represents a "non-ulcerated" area and (B) an "ulcerated" area. Stars indicate tumor ulceration. Black dotted lines depict the basement membrane zone (BMZ). Scale bars indicate 500 µm (upper panel) and 50 µm (lower panels). **B)** Mean tumor complexity in non-ulcerated and ulcerated areas (*N*≥6 tumor areas per condition) of 19 different BCC samples. Horizontal bars indicate the mean ±

SD, p-values were calculated by unpaired two-sided Student's *t* test. **C)** Representative scan image of an ulcerated BCC sample stained with DAPI. (A) represents a normal skin area, (B) a non-ulcerated area and (C) an ulcerated area. Stars indicate tumor ulceration. Scale bar indicates 200 µm. **D)** Representative scan images of ulcerated BCC samples stained with DAPI (blue), pan-cytokeratin (green), *GLI1* (purple) and *KRT6A* (yellow) in normal skin area (A), non-ulcerated area (B) and ulcerated area (C). White dotted lines depict the BMZ. Scale bars indicate 50 µm. **E)** Mean pixel intensity of *KRT6A* in non-ulcerated and ulcerated areas in N=7 ulcerated BCC samples. p-values were calculated by paired two-sided Student's *t* test and stars represent p-value <0.0017. **F)** Representative scan images of ulcerated BCC sections stained with DAPI (blue), pan-cytokeratin (green), *TIMP1* (red) and *CLDN4* (orange). White dotted lines depict the BMZ. Scale bars indicate 50 µm. **G)** Mean pixel intensity of *TIMP1* and *CLDN4* at 0 and 1 cell distance from BMZ in non-ulcerated and ulcerated areas measured in *N*≥450 cells/condition distributed over *N*=4 BCC samples. Horizontal bars indicate the mean ± SD. p-values were calculated one-way ANOVA and Tukey's multiple comparisons test (p-value: ns = non-significant, * <0.05, ** <0.01,*** <0.001). BMZ, basement membrane zone.

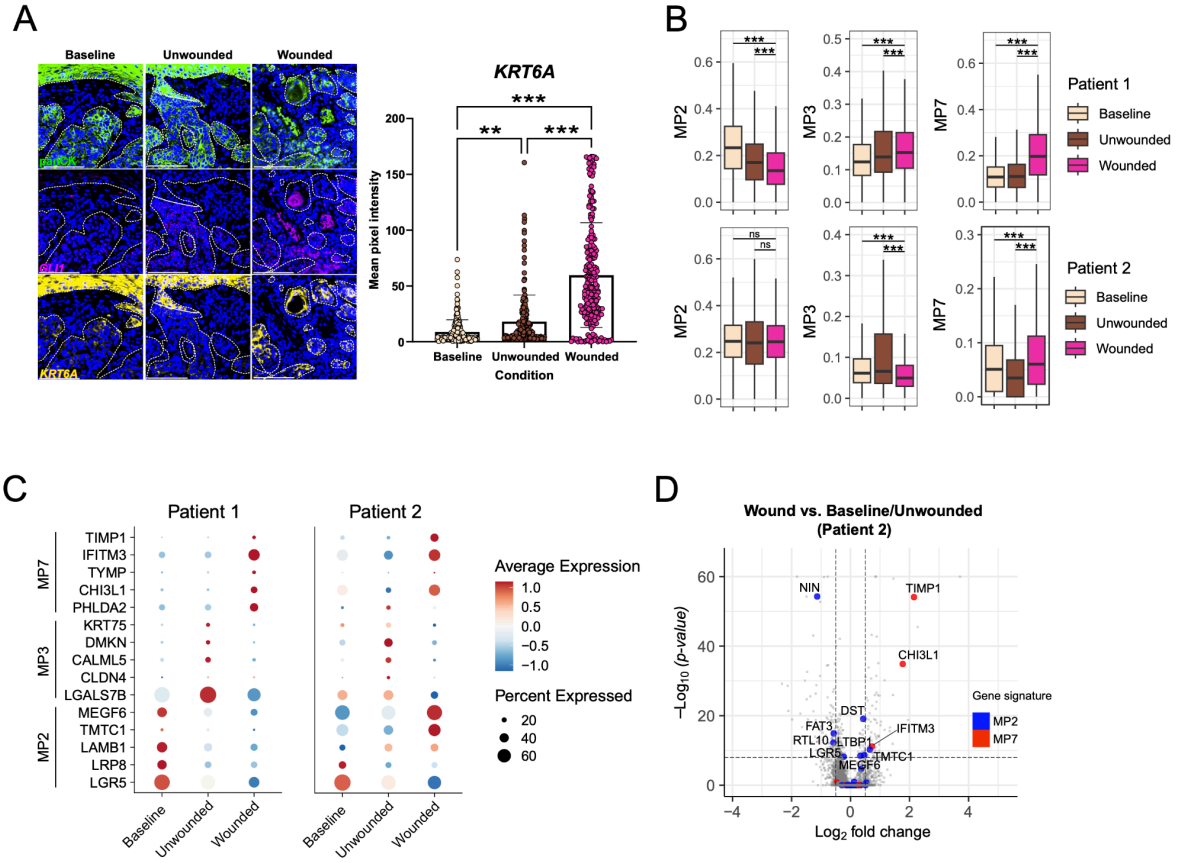

Figure S5. Transcriptional alterations induced by tumor wounding. A) Representative scan images of skin injury samples stained with DAPI (blue), pan-cytokeratin (green), *GLI1* (purple) and *KRT6A* (yellow). White dotted lines depict the basement membrane zone (BMZ). Scale bars indicate 100 µm. Bar graph represents the mean pixel intensity of *KRT6A* in Baseline, Unwounded and Wounded measured in *N*≥200 cells/condition distributed over *N*=3 BCC samples per condition. p-values were calculated by one-way ANOVA and Tukey's multiple comparisons test (p-value: ns = non-significant, * <0.05, ** <0.01, *** <0.001). **B)** Distribution of MP2 and MP3 (patients 1 and 2), and MP7 (patient 2) signature scores for cells in Baseline, Unwounded and Wounded samples. Stars indicate p-value < 0.001 (Wilcoxon rank-sum test). **C)** Scaled average expression of top 5 marker genes for the MP7, MP3 and MP2 (see Fig. 1) in Baseline, Unwounded and Wounded samples. **D)** Differentially expressed genes between Wounded sample vs. Baseline/Unwounded samples for Patient 4. Genes contained in MP2 and MP7 are highlighted. MP, meta-program.

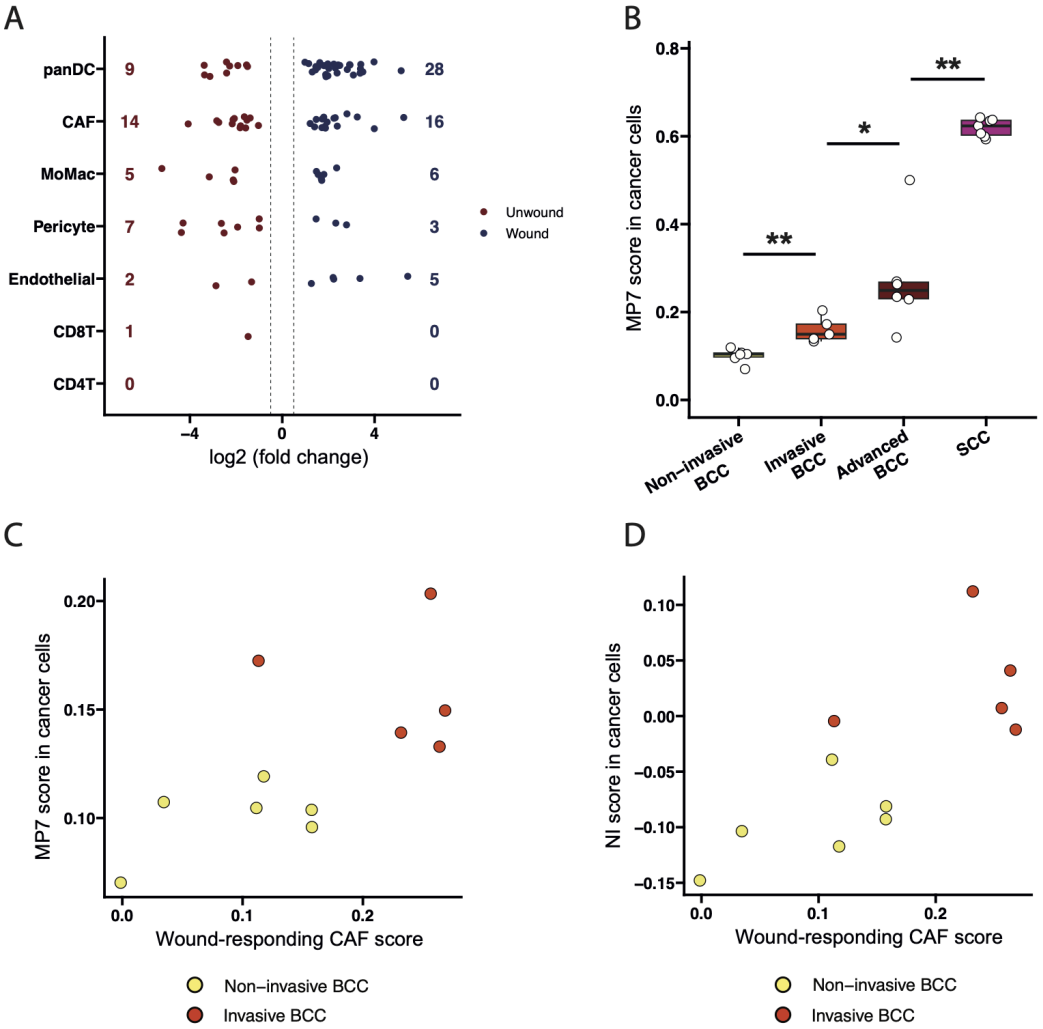

Figure S6. Wound-induced transcriptional alterations in the tumor microenvironment. A) Number of differentially expressed genes (adjusted p-value < 0.05 and |log2 fold-change| > 0.5; DEG), and log2 fold-change of the DEG in 7 major components of the TME. **B)** Mean MP7 score in cancer cells in human samples of different conditions (on the X-axis): non-cancer, adjacent skin samples ("Normal adjacent", N=6), non-invasive BCCs (N=6), invasive BCCs (N=5), advanced, Hedgehog inhibition (HHI)-therapy resistant BCC (N=7, samples from Yost et *al.* (2019); GSE123814), and squamous cell carcinomas (N=5, samples from Ji et *al.* (2020); GSE144236). **C)** Correlation between wound-responding CAF score (average of all CAFs by patient) and MP7 score (average of all cancer cells by patient), for invasive and non-invasive BCC samples. **D)** Correlation between wound-responding CAF score (average of all CAFs by patient) and NI.score (average of all cancer cells by patient), for invasive and non-invasive BCC samples. * adj. p-value <0.05, ** adj. p-value <0.01

Methods

RESOURCE AVAILABILITY

Lead contact

Further information and requests for resources and reagents should be directed to and will be fulfilled by the lead contact, François Kuonen (Francois.Kuonen@chuv.ch).

Materials availability

This study did not generate new unique reagents.

Data and code availability

Single-cell RNA sequencing data generated in this study have been deposited in the Gene Expression Omnibus database under accession codes GSE181907 and GSE266665. This paper also analyzes existing, publicly available data. The accession numbers for the datasets are listed in the key resources table.

The code to reproduce analyses and figures is available at https://github.com/CarmonaLab/Yerly_BCC_wounding.

EXPERIMENTAL MODEL AND STUDY PARTICIPANT DETAILS

Clinical samples

Studies were approved by the institutional review board of Lausanne University Hospital CHUV, and the local ethics committee, in accordance with the Helsinki Declaration (CER-VD 2020-02204 and 2021-01984). Written informed consent was obtained from each patient. Based on the principle of voluntary participation, no

compensation was provided to the patients in this study. Samples for scRNA-seq were collected from residual material of diagnostic biopsy or surgical piece and processed immediately after resection. Samples for RNA FISH were obtained from formalin-fixed paraffin-embedded tumor tissues. BCC samples referred to as “nodular” and “ulcerated” were identified unbiasedly based on the histopathological report registered between 2022 and 2023, and corresponding H&E slides were collected. Sample sizes are mentioned in the relative results section. Patient characteristics are available in **Table S1**.

METHOD DETAILS

Tissue dissociation and single cell sorting

Fresh tumor tissues were transported in Medium 154CF (Gibco™, M-154CF-500) on ice to preserve viability. The tumor tissues were then minced with scalpels to pieces < 1mm3 and transferred in 10 mL Medium 154CF with collagenase (5 mg/mL, (Gibco™, 17018029)) to digest the tissue. The mixture was incubated for 90 min at 37°C with manual shaking every 10 min. Then, 5 mL 0.05 % trypsin-EDTA (Gibco™, 25300-054) was added to the mixture and the digestion cocktail was incubated again for 10 min at 37°C. After incubation, the mixture was centrifuged at 500 g for 5 min at 4°C. 5 mL 10% fetal bovine serum (FBS, (VWR, S181B-500)) was added to the pellet to inhibit the digestion enzymes. The mixture was centrifuged at 500 g for 5 min at 4°C. Cells were suspended in 10 mL MACS buffer (2% FBS, 2 mM EDTA (Promega, V4231) diluted in phosphate-buffered saline (PBS) (Bichsel, 100 0 324)). The cell suspension was then filtered through a 70-µm cell strainer (Plexus-Santé, PL000223). Afterwards, the cells were stained with SYTO™ 13 Green Fluorescent Nucleic Acid Stain (Invitrogen, S7575) and SYTOX™ Orange Nucleic Acid Stain

(Invitrogen, S11368) for viability assessment. Stained cells were suspended in MACS buffer. Single living cells (SYTO™ green^{Pos}, SYTOX™ orange^{Neg}) were then FACS sorted and collected in collecting medium (10% FBS, 2 mM EDTA in PBS). Sorted cells were centrifuged at 500 g for 5 min at 4°C. The cells were then suspended in 10% FBS and counted. The cell suspension was centrifuged at 500 g for 5 min at 4°C. Cells were suspended in the appropriate volume of 10% FBS to obtain a final concentration of approximately 1,000 cells/µl.

scRNA-seq processing (Emulsion / Library preparation / Sequencing)

Single-cell mRNA capture and sequencing were performed immediately after reaching the optimal cell suspension by the Lausanne Genomic Technologies Facility (GTF, https://wp.unil.ch/gtf/) using the Chromium Next GEM single cell 3' v3.1 reagent kit (10x Genomics) following the manufacturer's protocol. The target number of captured cells was 10,000 per sample. Sequencing libraries were prepared per the manufacturer's protocol. Sequencing was performed on Illumina NovaSeq 6000 v1.5 (Novaseq Control Software v.1.7.5 for BCC6 and BCC7 or v.1.8.1 for Baseline1/2, Wound1/2 and Unwound1/2) flow cells for 28-10-10-90 cycles (read1 - index i7 - index i5 - read2) with 1% PhiX spike in at a median depth of 23,490 reads/cell for BCC6, 18,397 reads/cell for BCC7, 25,111 reads/cell for Baseline1, 22,592 reads/cell for Wound1, 25,463 reads/cell for Unwound1, 19,049 reads/cell for Basline2, 17,550 reads/cell for Wound2, 16,983 reads/cell for Unwound2. Sequencing data were demultiplexed using the bcl2fastq2 Conversion Software (v. 2.20, Illumina) and primary data analysis performed with the Cell Ranger Gene Expression pipeline (v.6.0.0 for BCC6 and BCC7 and v.7.1.0 for Baseline1/2, Wound1/2 and Baseline1/2, 10x Genomics

(https://www.10xgenomics.com/support/software/cell-ranger/downloads) using the human GRCh38 genome reference (refdata-gex-GRCh38-2020-A).

scRNA-seq data processing and quality control

Bioinformatics analyses for scRNA-seq data generated in this study, as well as meta-analyses of previously published datasets (GSE181907[9], E-MTAB-13085[10], GSE144236[26], GSE123814[23]), were performed using the Seurat framework[57]. To make samples from different sources comparable, we harmonized gene names to a common dictionary of Ensembl BioMart gene symbols[58]. Low-quality transcriptomes were excluded from the analysis by filtering out cells with extreme numbers of UMI counts (<600 and >25000), number of detected genes (<500 and >6000), more than 20% of mitochondrial genes, or more than 15% of genes associated with tissue dissociation[59]. Dimensionality reduction was performed using the top 2000 variable genes, and subsequently applying principal component analysis (PCA). The 30 PCA components with highest explained variance were used for unsupervised clustering and for further dimensionality reduction for purely visualization purposes by Uniform Manifold Approximation and Projection (UMAP). Preliminary, automated cell type annotation was obtained using the scGate method and the "TME_HiRes" model (https://github.com/carmonalab/scGate_models) [25], subsequently refining annotations by majority vote of the automated labels in unsupervised clusters (**Fig. S1**). As scGate does not provide models for cancer cells, malignant and normal keratinocytes were identified as outlined in the following section.

Identification of malignant cells from scRNA-seq data

We employed a three-tier procedure to distinguish malignant cells from normal keratinocytes, based on *i)* patient mixing by cell type, *ii)* BCC signature scoring and *iii)* copy-number alterations (CNA). Patient mixing, quantified by the Local Inverse

Simpson's score (LISI) score[60], aims at evaluating how well mixed cells from different samples are when embedded together. Because cancer cells tend to have altered gene regulation and abnormal expression, they can be expected to display more sample-specific features and, as a consequence, lower LISI score (see e.g. **Fig S1B** and **S1F**). Second, specific cancer types can display patterns of genes which are consistently differentially expressed compared to healthy cells. In this study, we applied a signature composed of genes previously identified as overexpressed in BCC (*PTCH1*, *GLI1*, *GLI2*, *SPON2*, *HHIP*, *MYCN*) and scored this gene set using UCell[61] (see e.g. **Fig. S1C** and **S1G**). Third, we applied inferCNV[62] for copy-number alteration analysis to detect chromosomal regions with altered expression patterns compared to reference transcriptomes. Clustering of CNA profiles of cancer cells and normal keratinocytes (using T cells as a reference transcriptome) confirmed that malignant cells had consistent alterations that allowed distinguishing them from healthy keratinocytes (see e.g. **Fig. S1D** and **S1H**).

Characterization of cancer gene programs by NMF

To discover gene programs across multiple BCC samples, we applied non-negative matrix factorization (NMF) on 11 samples for which at least 100 cancer cells were available. We implemented our multi-sample NMF discovery algorithm in a R package (GeneNMF), available on the CRAN repository at: https://cran.r-project.org/package=GeneNMF. We describe the algorithm in detail in **Additional Resources**, but briefly, GeneNMF performs factorization of individual samples and for multiple values of the target number of gene programs. Then, it determines clusters of similar programs which are consistently identified across multiple samples. The consensus signatures of such clusters of programs are termed meta-programs (MP). We ran GeneNMF with k=4:9 (number of target NMF

components for each dataset between 4 to 9) on the top 2000 variable genes across samples, and asked for 10 target MPs with min.confidence=0.3. We further filtered GeneNMF results by dropping MPs with fewer than 5 genes, negative average silhouette coefficient, or sample coverage lower than 40%. On the 7 high-confidence MPs, we calculated MP signatures scores by applying the UCell method[61] and determined differentially expressed genes (DEG) between the top 20% and bottom 20% scoring cells; we only retained genes from the MP sets that were also found among the DEGs, to construct gene sets with specific expression for each MP.

Nodular-to-infiltrative (NI) signature for single-cell data

To place cells on a nodular-to-infiltrative axis, we used previously published signatures of nodular and infiltrative cancer cell niches (T^{inf} and T^{nod} respectively) derived from GeoMx spatial transcriptomics[9]. We calculated UCell scores for the T^{inf} and T^{nod} gene sets, and combined them into a single "Nodular-to-infiltrative score" defined as NI.score = UCell(T^{inf}) - UCell(T^{nod}). This score varies between -1 (fully nodular) to +1 (fully infiltrative).

To identify globally non-invasive and invasive BCC tumors, samples from 11 patients having at least 100 cancer cells were classified using the following criteria. The average NI score by patient was calculated on their cancer cells. Based on the average NI score, patients were split into two groups of equal size: patients with an average NI score above the median were classified as invasive BCC, while those with an average NI score below the median were classified as non-invasive BCC (**Fig. S6C**).

Linear models of NI score

To analyze the relation between meta-programs and NI status, we constructed a linear model to predict the NI score from a multi-variate combination of MP signature

scores. We applied the “lm” R function to fit a linear model with the following formula: *NI.score ~ MP[1-7] + Patient*, aimed at predicting the NI score from the MP signature scores while accounting for the sample of origin (Patient). Because “Patient” is a categorical variable with n levels, it must be converted into a numerical contrast matrix of n-1 levels (commonly known as “dummy coding”); therefore the coefficient estimates will be reported for n-1 patients. We note that MP signature scores are not strictly independent, with potential multicollinearity effects in the construction of a regression model. In particular, MP7 and MP3 scores were shown to be the most strongly correlated variables (**Fig. 2A**). To assess the contribution of MPs to a predictive model of NI scores in the absence of MP7, we fit an alternative model based on the remaining six MPs with the formula: *NI.score ~ MP[1-6] + Patient*. We observed that, while most other coefficient estimates remained largely stable, the contribution for MP3 went from negative to positive in absence of MP7 in the model (cf. **Fig. 1F** and **Fig. S2C**). This is in agreement with the observation that MP3 has positive univariate correlation with the NI score, but that MP7 is the strongest predictor for the NI score.

Definition and scoring of “wound-responding CAF” signature

Cancer-associated fibroblasts (CAF) were identified using the scGate[25] method with specific fibroblast markers, excluding pericytes (*PDGFA*$^{+}$, *FBLN1*$^{+}$, *FBLN2*$^{+}$, *COL5A1*$^{+}$, *LUM*$^{+}$, *CFD*$^{+}$, *RGS5*$^{-}$, *NOTCH3*$^{-}$, *MYOT*$^{-}$) and aggregated into a pseudo-bulk expression matrix for each sample.

Paired differential expression analysis was performed using the DESeq2 package[63] on pseudo-bulk samples, comparing wounded vs. unwounded and baseline conditions. Genes with a log2 fold change > 0.5 and adjusted p-value < 0.05 were

identified as part of the wound signature, while those with a log2 fold change < -0.5 and adjusted p-value < 0.05 constituted the unwound/baseline signature (**Table S3**).

These signatures were scored using UCell[61] on CAFs from retrospective cohort single-cell samples (GSE181907[9], E-MTAB-13085[10], GSE144236[26], GSE123814[23]) previously classified by scGate[25]. The "wound-responding CAF" score was calculated by subtracting the unwound/baseline signature score from the wound signature score in each cell, defined as: Wound-responding CAF score = UCell(CAF^{wound}) - UCell($CAF^{unwound/baseline}$).

The score was computed on fibroblasts from different datasets: non-cancer, adjacent skin samples ("Normal adjacent", N=6) obtained from GSE144236, Hedgehog inhibition (HHI)-therapy resistant BCC (N=7, samples from[23]; GSE123814), squamous cell carcinomas (N=5, samples from[26]; GSE144236), and BCC tumors (N=11, samples from GSE181907[9] and E-MTAB-13085[10]) .

Immunofluorescence and Fluorescence *In Situ* Hybridization (FISH) co-detection

FFPE skin blocks were cut and 5-µm sections were mounted onto Superfrost Plus® microscope slides. FFPE skin sections were heated 10 min at 60°C. Slides were deparaffinized in 2 xylene baths of 3 min, then rehydrated in an ethanol gradient from 100% EtOH (2 baths of 3 min), followed by 95% EtOH (3 min) and 70% EtOH (3 min). Slides were then washed in distilled water. RNAscope® Hydrogen Peroxide (ACD, 323100) was added to the tissue sections and slides were incubated for 10 min at room temperature. Slides were then washed for 5 min in distilled water followed by 5 min in PBS 1X. Antigen retrieval was done in 1X Co-detection Target Retrieval buffer (ACD, 323180) pre-warmed at 100°C for 15 min. Slides were then washed twice 2 min in distilled water and 2 min in 1X Phosphate Buffered Saline with

0.1% Tween-20 (PBS-T) (PBS: Bichsel, 100 0 324, Tween-20: Sigma, P1379-500ML). Each tissue section was then covered with the primary antibody solution (Monoclonal antibody to human cytokeratin (pan) (clone Lu-5) (BMA Biomedicals, T-1302) diluted 1:250 in Co-Detection Antibody Diluent (ACD, 323180)) and incubated 2 hours at room temperature in a humidified box. Following primary antibody incubation, slides were washed twice in PBS-T for 2 min. Slides were then fixed for 30 min in Buffered Zinc Formalin (Thermo Scientific, 5701ZF) at room temperature. After fixation, slides were wash four times in PBS-T for 2 min. Protease treatment, probe hybridization, amplifications and stainings were performed with the RNAscope® Multiplex Fluorescent Reagent Kit v2 Assay kit (ACD, 323100) according to the manufacturer's instructions. After the final *in situ* hybridization horseradish peroxidase (HRP)-blocker step, each tissue section was covered with the secondary antibody dilution (F(ab')2-Goat anti-Mouse IgG (H+L) Cross-Adsorbed Secondary Antibody, Alexa Fluor™ 488 (Thermo Fisher Scientific, A-11017) diluted 1:500 in Co-Detection Antibody Diluent) for 30 min at room temperature. Slides were then washed twice for 2 min in PBS-T. Finally, slides were mounted with mounting medium with DAPI-Aqueous Fluoroshield (abcam, ab104139). The slides were acquired with Pannoramic 250 slide scanner and processed using SlideViewer 2.5.0.143918 and (Fiji Is Just) ImageJ softwares. The mean pixel intensity of the different FISH stainings was measured in individual cells with Fiji is just ImageJ. Chosen areas and distribution over samples are described in the legend of the corresponding figures.

Tumor complexity

Tumor complexity was calculated by dividing the perimeter by the area (measured with Fiji is just ImageJ) of tumoral structures in similar BCC samples as the ones used for immunofluorescence and FISH staining.

ADDITIONAL RESOURCES

GeneNMF package

We developed an R package, GeneNMF, to streamline the identification of gene programs from scRNA-seq data using non-negative matrix factorization (NMF). NMF is a dimensionality reduction technique that aims at decomposing a high-dimensional data matrix **A** into the product of two matrices **W** and **H** such that **A** ≅ **WH**, with the constraints that all elements in the three matrices should be zero or positive. In the case of scRNA-seq data, **A** is the observed gene expression matrix of size g x c (where g is the number of genes and c the number of cells); **H** is the embedding matrix of size k x c (where k is the number of gene programs) containing the coordinates of cells in the low dimensional space; and **W** is the feature loading matrix of size g x k, containing the coefficients of each gene in each program.

Given a list of expression matrices, one for each sample, GeneNMF performs NMF decomposition individually for each sample using the RccpML library (https://CRAN.R-project.org/package=RcppML). Critical parameters are the set of genes used as input (by default the top 2000 variable genes); the minimum and maximum average log-expression value for including genes in the decomposition; and the number of components **k**, corresponding to the target number of gene programs for a single run. The multiNMF() function of GeneNMF allows specifying a range of values for **k**, prompting the method to generate a NMF decomposition for

each value of **k**, for each sample. The method then extracts the most program-specific genes using the extractFeatures() methods implemented in the "NMF" package[64]. Similarly to the approach by Gavish et *al.*[11], GeneNMF then clusters gene programs by the fraction of shared genes, as can be quantified using the Jaccard similarity coefficient. The consensus of the gene sets in any given cluster of programs is termed meta-program (MP). Several metrics are generated by GeneNMF for each MP. In particular, the average Jaccard index informs on the internal consistency of individual programs within a MP; the silhouette width coefficient quantifies whether a MPs is specific, or whether it shares genes with other MPs; sample coverage quantifies the proportion of samples in which the MP was detected. These metrics can be used downstream to evaluate the quality of the decomposition, assess properties of individual MPs, and filter out inconsistent or redundant MPs.

We note that NMF has been previously applied for the decomposition of single-cell data[11,65,66]. In particular, the consensus NMF (cNMF) method[66] addressed a potential limitation of NMF, namely its reliance on stochastic optimization algorithms and consequent non-deterministic nature. cNMF introduced the idea of performing multiple decomposition replicates from different initialization seeds, and then calculating a consensus of the resulting multiple solutions. Inspired by the work of Gavish et *al.*[11], GeneNMF extends the consensus NMF approach to span multiple values of **k,** a crucial parameter that determines the target number of programs for each NMF run, and which is generally a priori unknown. Importantly, GeneNMF can interact directly with the Seurat infrastructure, making it very straightforward to incorporate in analysis pipelines for single-cell analysis.

References

1. Cameron, M. C. *et al.* Basal cell carcinoma: Epidemiology; pathophysiology; clinical and histological subtypes; and disease associations. *J. Am. Acad. Dermatol.* **80**, 303–317 (2019).
2. Crowson, A. N. Basal cell carcinoma: biology, morphology and clinical implications. *Mod. Pathol.* **19**, S127–S147 (2006).
3. Hanahan, D. Hallmarks of Cancer: New Dimensions. *Cancer Discov.* **12**, 31–46 (2022).
4. Caccialanza, M., Piccinno, R., Çuka, E., Alberti Violetti, S. & Rozza, M. Radiotherapy of morphea-type basal cell carcinoma: results in 127 cases. *J. Eur. Acad. Dermatol. Venereol.* **28**, 1751–1755 (2014).
5. Pich-Bavastro, C. *et al.* Activin A-mediated polarization of cancer-associated fibroblasts and macrophages confers resistance to checkpoint immunotherapy in skin cancer. *Clin. Cancer Res.* CCR-23-0219 (2023) doi:10.1158/1078-0432.CCR-23-0219.
6. Bonilla, X. *et al.* Genomic analysis identifies new drivers and progression pathways in skin basal cell carcinoma. *Nat. Genet.* **48**, 398–406 (2016).
7. Villani, R. *et al.* Subtype-Specific Analyses Reveal Infiltrative Basal Cell Carcinomas Are Highly Interactive with their Environment. *J. Invest. Dermatol.* **141**, 2380–2390 (2021).
8. Kuonen, F. *et al.* TGFβ, Fibronectin and Integrin α5β1 Promote Invasion in Basal Cell Carcinoma. *J. Invest. Dermatol.* **138**, 2432–2442 (2018).
9. Yerly, L. *et al.* Integrated multi-omics reveals cellular and molecular interactions governing the invasive niche of basal cell carcinoma. *Nat. Commun.* **13**, 4897 (2022).
10. Ganier, C. *et al.* Multiscale spatial mapping of cell populations across anatomical sites in healthy human skin and basal cell carcinoma. *Proc. Natl. Acad. Sci.* **121**, e2313326120 (2024).
11. Gavish, A. *et al.* Hallmarks of transcriptional intratumour heterogeneity across a thousand tumours. *Nature* **618**, 598–606 (2023).
12. Wong, S. Y. *et al.* Primary cilia can both mediate and suppress Hedgehog pathway–dependent tumorigenesis. *Nat. Med.* **15**, 1055–1061 (2009).
13. Joost, S. *et al.* Single-Cell Transcriptomics of Traced Epidermal and Hair Follicle Stem Cells Reveals Rapid Adaptations during Wound Healing. *Cell Rep.* **25**, 585-597.e7 (2018).
14. Peris, K. *et al.* European consensus-based interdisciplinary guideline for diagnosis and treatment of basal cell carcinoma—update 2023. *Eur. J. Cancer* **192**, 113254 (2023).
15. Altamura, D. *et al.* Dermatoscopy of basal cell carcinoma: Morphologic variability of global and local features and accuracy of diagnosis. *J. Am. Acad. Dermatol.* **62**, 67–75 (2010).
16. Gershenwald, J. E. & Scolyer, R. A. Melanoma Staging: American Joint Committee on Cancer (AJCC) 8th Edition and Beyond. *Ann. Surg. Oncol.* **25**, 2105–2110 (2018).
17. Naseri, S. *et al.* Tumor Ulceration, Reduced Infiltration of CD8-Lymphocytes, High Neutrophil-to-CD8-Lymphocyte Ratio and Absence of MC Virus are Negative Prognostic Markers for Patients with Merkel Cell Carcinoma. *Cancers* **12**, 888 (2020).
18. Pastar, I. *et al.* Epithelialization in Wound Healing: A Comprehensive Review. *Adv. Wound Care* **3**, 445–464 (2014).
19. Lei, V. *et al.* Skin Injury Activates a Rapid TRPV1-Dependent Antiviral Protein Response. *J. Invest. Dermatol.* **142**, 2249-2259.e9 (2022).
20. Leonardo, T. R., Shi, J., Chen, D., Trivedi, H. M. & Chen, L. Differential Expression and Function of Bicellular Tight Junctions in Skin and Oral Wound Healing. *Int. J. Mol. Sci.* **21**, 2966 (2020).
21. Ramey-Ward, A. N., Walthall, H. P., Smith, S. & Barrows, T. H. Human keratin matrices promote wound healing by modulating skin cell expression of cytokines and growth factors. *Wound Repair Regen.* **32**, 257–267 (2024).
22. Gendronneau, G. *et al.* Galectin-7 in the Control of Epidermal Homeostasis after Injury. *Mol. Biol. Cell* **19**, 5541–5549 (2008).
23. Yost, K. E. *et al.* Clonal replacement of tumor-specific T cells following PD-1 blockade. *Nat. Med.* **25**, 1251–1259 (2019).
24. Winge, M. C. G. *et al.* Advances in cutaneous squamous cell carcinoma. *Nat. Rev. Cancer* **23**, 430–449 (2023).
25. Andreatta, M., Berenstein, A. J. & Carmona, S. J. scGate: marker-based purification of cell types from heterogeneous single-cell RNA-seq datasets. *Bioinformatics* **38**, 2642–2644 (2022).
26. Ji, A. L. *et al.* Multimodal Analysis of Composition and Spatial Architecture in Human Squamous Cell Carcinoma. *Cell* **182**, 497-514.e22 (2020).
27. MacCarthy-Morrogh, L. & Martin, P. The hallmarks of cancer are also the hallmarks of wound healing. *Sci. Signal.* **13**, eaay8690 (2020).
28. Özyazgan, İ. & Kontaş, O. Previous injuries or scars as risk factors for the development of basal cell carcinoma. *Scand. J. Plast. Reconstr. Surg. Hand Surg.* **38**, 11–15 (2004).

29. Fine, J.-D., Johnson, L. B., Weiner, M., Li, K.-P. & Suchindran, C. Epidermolysis bullosa and the risk of life-threatening cancers: The National EB Registry experience, 1986-2006. *J. Am. Acad. Dermatol.* **60**, 203–211 (2009).
30. Fine, J.-D. *et al.* Inherited epidermolysis bullosa: Updated recommendations on diagnosis and classification. *J. Am. Acad. Dermatol.* **70**, 1103–1126 (2014).
31. Hartnett, L. & Egan, L. J. Inflammation, DNA methylation and colitis-associated cancer. *Carcinogenesis* **33**, 723–731 (2012).
32. Manuel A Valenzuela, J. C. & N, A. F. Q. Helicobacter pylori-induced inflammation and epigenetic changes during gastric carcinogenesis. *World J. Gastroenterol.* **21**, 12742–12756 (2015).
33. Hill, W. *et al.* Lung adenocarcinoma promotion by air pollutants. *Nature* **616**, 159–167 (2023).
34. Antonio, N. *et al.* The wound inflammatory response exacerbates growth of pre-neoplastic cells and progression to cancer. *EMBO J.* **34**, 2219–2236 (2015).
35. Garlick, J. A. & Taichman, L. B. Fate of human keratinocytes during reepithelialization in an organotypic culture model. *Lab. Invest.* **70**, 916–24 (1994).
36. Gedeon Matoltsy, A. & Viziam, C. B. Further Observations on Epithelialization of Small Wounds. *J. Invest. Dermatol.* **55**, 20–25 (1970).
37. Park, S. *et al.* Tissue-scale coordination of cellular behaviour promotes epidermal wound repair in live mice. *Nat. Cell Biol.* **19**, 155–163 (2017).
38. Aragona, M. *et al.* Defining stem cell dynamics and migration during wound healing in mouse skin epidermis. *Nat. Commun.* **8**, 14684 (2017).
39. Koivisto, L., Häkkinen, L. & Larjava, H. Re-epithelialization of wounds. *Endod. Top.* **24**, 59–93 (2011).
40. Slack, R. J., Macdonald, S. J. F., Roper, J. A., Jenkins, R. G. & Hatley, R. J. D. Emerging therapeutic opportunities for integrin inhibitors. *Nat. Rev. Drug Discov.* **21**, 60–78 (2022).
41. Martin, P. Wound Healing--Aiming for Perfect Skin Regeneration. *Science* **276**, 75–81 (1997).
42. Bansaccal, N. *et al.* The extracellular matrix dictates regional competence for tumour initiation. *Nature* **623**, 828–835 (2023).
43. Katikaneni, A. *et al.* Lipid peroxidation regulates long-range wound detection through 5-lipoxygenase in zebrafish. *Nat. Cell Biol.* **22**, 1049–1055 (2020).
44. Uderhardt, S., Martins, A. J., Tsang, J. S., Lämmermann, T. & Germain, R. N. Resident Macrophages Cloak Tissue Microlesions to Prevent Neutrophil-Driven Inflammatory Damage. *Cell* **177**, 541-555.e17 (2019).
45. Razzell, W., Evans, I. R., Martin, P. & Wood, W. Calcium Flashes Orchestrate the Wound Inflammatory Response through DUOX Activation and Hydrogen Peroxide Release. *Curr. Biol.* **23**, 424–429 (2013).
46. Gurtner, G. C., Werner, S., Barrandon, Y. & Longaker, M. T. Wound repair and regeneration. *Nature* **453**, 314–321 (2008).
47. Izikson, L., Seyler, M. & Zeitouni, N. C. Prevalence of Underdiagnosed Aggressive Non-Melanoma Skin Cancers Treated with Mohs Micrographic Surgery: Analysis of 513 Cases. *Dermatol. Surg.* **36**, 1769 (2010).
48. Haws, A. L., Rojano, R., Tahan, S. R. & Phung, T. L. Accuracy of biopsy sampling for subtyping basal cell carcinoma. *J. Am. Acad. Dermatol.* **66**, 106–111 (2012).
49. Mosterd, K. *et al.* Correlation between histologic findings on punch biopsy specimens and subsequent excision specimens in recurrent basal cell carcinoma. *J. Am. Acad. Dermatol.* **64**, 323–327 (2011).
50. Dik, E. A. *et al.* Poor Correlation of Histologic Parameters Between Biopsy and Resection Specimen in Early Stage Oral Squamous Cell Carcinoma. *Am. J. Clin. Pathol.* **144**, 659–666 (2015).
51. Daveau, C. *et al.* Histological grade concordance between diagnostic core biopsy and corresponding surgical specimen in HR-positive/HER2-negative breast carcinoma. *Br. J. Cancer* **110**, 2195–2200 (2014).
52. Kim, Y. J. *et al.* Histologic diagnosis based on forceps biopsy is not adequate for determining endoscopic treatment of gastric adenomatous lesions. *Endoscopy* **42**, 620–626 (2010).
53. Lim, H. *et al.* Discrepancy between endoscopic forceps biopsy and endoscopic resection in gastric epithelial neoplasia. *Surg. Endosc.* **28**, 1256–1262 (2014).
54. Fiechter, S. *et al.* Facial basal cell carcinomas recurring after photodynamic therapy: a retrospective analysis of histological subtypes. *Dermatol. Basel Switz.* **224**, 346–351 (2012).
55. Boulinguez, S. *et al.* Histological evolution of recurrent basal cell carcinoma and therapeutic implications for incompletely excised lesions. *Br. J. Dermatol.* **151**, 623–626 (2004).

56. Menn, H., Robins, P., Kopf, A. W. & Bart, R. S. The Recurrent Basal Cell Epithelioma: A Study of 100 Cases of Recurrent, Re-treated Basal Cell Epitheliomas. *Arch. Dermatol.* **103**, 628–631 (1971).
57. Hao, Y. *et al.* Integrated analysis of multimodal single-cell data. *Cell* **184**, 3573-3587.e29 (2021).
58. Martin, F. J. *et al.* Ensembl 2023. *Nucleic Acids Res.* **51**, D933–D941 (2023).
59. van den Brink, S. C. *et al.* Single-cell sequencing reveals dissociation-induced gene expression in tissue subpopulations. *Nat. Methods* **14**, 935–936 (2017).
60. Korsunsky, I. *et al.* Fast, sensitive and accurate integration of single-cell data with Harmony. *Nat. Methods* **16**, 1289–1296 (2019).
61. Andreatta, M. & Carmona, S. J. UCell: Robust and scalable single-cell gene signature scoring. *Comput. Struct. Biotechnol. J.* **19**, 3796–3798 (2021).
62. Tirosh, I. *et al.* Dissecting the multicellular ecosystem of metastatic melanoma by single-cell RNA-seq. *Science* **352**, 189–196 (2016).
63. Love, M. I., Huber, W. & Anders, S. Moderated estimation of fold change and dispersion for RNA-seq data with DESeq2. *Genome Biol.* **15**, 550 (2014).
64. Gaujoux, R. & Seoighe, C. A flexible R package for nonnegative matrix factorization. *BMC Bioinformatics* **11**, 367 (2010).
65. Barkley, D. *et al.* Cancer cell states recur across tumor types and form specific interactions with the tumor microenvironment. *Nat. Genet.* **54**, 1192–1201 (2022).
66. Kotliar, D. *et al.* Identifying gene expression programs of cell-type identity and cellular activity with single-cell RNA-Seq. *eLife* **8**, e43803 (2019).
67. Schindelin, J. *et al.* Fiji: an open-source platform for biological-image analysis. *Nat. Methods* **9**, 676–682 (2012).

KEY RESOURCES TABLE

REAGENT or RESOURCE	SOURCE	IDENTIFIER
Antibodies		
Mouse Anti-pan-Cytokeratin Monoclonal Antibody, Unconjugated, Clone Lu-5	BMA Biomedicals	Cat# T-1302, RRID:AB_1227343
F(ab')2-Goat anti-Mouse IgG (H+L) Cross-Adsorbed Secondary Antibody, Alexa Fluor™ 488	Thermo Fisher Scientific	Cat# A-11017 RRID:AB_2534084
Biological samples		
Human basal cell carcinoma tissues	Centre hospitalier universitaire vaudois (CHUV), dermatological biobank	This paper
Chemicals, peptides, and recombinant proteins		
SYTO™ Green Fluorescent Nucleic Acid Stains	Invitrogen™	Cat# S7575
SYTOX™ Orange Nucleic Acid Stain – 5mM Solution in DMSO	InvitrogenTM	Cat# S11368
Opal 650 Reagent	Akoya Biosciences	Cat# FP1496001KT
Opal 570 Reagent	Akoya Biosciences	Cat# FP1488001KT
RNAscope™ Probe Hs-KRT6A-C3	ACD	Cat# 520721-C3
RNAscope™ Probe- Hs-TIMP1	ACD	Cat# 567841
RNAscope™ Probe- Hs-TIMP1-C2	ACD	Cat# 567841-C2
RNAscope™ Probe- Hs-GLI1	ACD	Cat# 310991
RNAscope™ Probe- Hs-CLDN4-C2	ACD	Cat# 421041-C2
Mounting Medium With DAPI - Aqueous, Fluoroshield	Abcam	Ab104139
Critical commercial assays		
RNA-Protein Co-Detection Ancillary Kit	ACD	Cat# 323180
RNAscope® Multiplex Fluorescent Reagent Kit v2	ACD	Cat# 323100
Chromium Next GEM single cell 3' v3.1 reagent kit	10x Genomics	PN-1000121
Novaseq 6000 S2 Reagent Kit v1.5 (200 cycles)	Illumina	Cat# 20028315
Novaseq 6000 S4 Reagent Kit v1.5 (300 cycles)	Illumina	Cat# 20028313
Deposited data		
BCC cohort	Yerly L. et *al.*[9]	GSE181907
BCC cohort (GeoMX)	Yerly L. et *al.*[9]	GSE210648
BCC cohort	Ganier C. et *al.*[10]	E-MTAB-13085
BCC cohort (wounding experiment)	This paper	GSE266665
Advanced BCC cohort	Yost K.E. et *al.*[23]	GSE123814
SCC cohort	Ji A.L. et *al.*[26]	GSE144236
human GRCh38 genome reference	10X Genomics	refdata-gex-GRCh38-2020-A
Software and algorithms		
SlideViewer version 2.5.b	3DHisTech	https://www.3dhistech.com/
(Fiji Is Just) ImageJ version 1.52h.b	Schindelin J et *al.*[67]	https://imagej.net/software/fiji/
GraphPad Prism 10.1.2	GraphPad Software, Boston, Massachusetts USA	https://www.graphpad.com/
R	v 4.3.2	https://cran.r-project.org/
Seurat	CRAN (v 5.0.3)	https://CRAN.R-project.org/package=Seurat

GeneNMF	CRAN (v 0.4.0)	https://CRAN.R-project.org/package=GeneNMF
UCell	Bioconductor (v 2.7.7)	https://bioconductor.org/packages/UCell/
scGate	CRAN (v 1.6.0)	https://CRAN.R-project.org/package=scGate
inferCNV	Bioconductor (v 1.18.0)	https://bioconductor.org/packages/infercnv/
Novaseq Control Software version 1.7.5	Illumina	https://support.illumina.com/downloads/novaseq-control-software-v1-7-5.html
Novaseq Control Software version 1.8.1	Illumina	https://support.illumina.com/downloads/novaseq-control-software-v1-8.html
bcl2fastq2 Conversion Software version 2.20	Illumina	https://support.illumina.com/downloads/bcl2fastq-conversion-software-v2-20.html
Cell Ranger pipeline version 6.0.0	10X Genomics	https://www.10xgenomics.com/support/software/cell-ranger/downloads
Cell Ranger pipeline version 7.1.0	10X Genomics	https://www.10xgenomics.com/support/software/cell-ranger/downloads